The Southern SHARC catalogue: a ROSAT survey for distant galaxy clusters

Article (Published Version)

Mon. Not. R. Astron. Soc. **341,** 1093–1108 (2003)

The Southern SHARC catalogue: a *ROSAT* survey for distant galaxy clusters

D. J. Burke,[1⋆] C. A. Collins,[2] R. M. Sharples,[3] A. K. Romer[4] and R. C. Nichol[4]

[1]*Harvard-Smithsonian Center for Astrophysics, 60 Garden Street, Cambridge, MA 02138, USA*
[2]*Astrophysics Research Institute, Liverpool John Moores University, 12 Quays House, Egerton Wharf, Birkenhead CH41 1LD*
[3]*Department of Physics, University of Durham, South Road, Durham DH1 3LE*
[4]*Department of Physics, Carnegie Mellon University, 5000 Forbes Avenue, Pittsburgh, PA 15213, USA*

Accepted 2002 December 14. Received 2002 December 4; in original form 2002 August 27

ABSTRACT

X-ray selection provides a way of creating well-defined samples of distant clusters free from projection effects and with a well-understood selection function. This paper describes the creation of one such catalogue – the Southern Serendipitous High-redshift Archival *ROSAT* Cluster (SHARC) survey – which covers an area of 17.7 deg^2 and consists of 32 clusters with redshifts between 0.05 and 0.7 and X-ray luminosities between 7×10^{42} and 4×10^{44} erg s^{-1}: the high-redshift subsample contains 16 clusters with $z \geqslant 0.3$ and X-ray luminosities greater than 2×10^{43} erg s^{-1} (luminosities are quoted for the 0.5–2.0 keV energy band). The catalogue is in good agreement with those of other *ROSAT* cluster surveys for those fields in common. The high-redshift sample is consistent with there being no evolution in the cluster X-ray luminosity function at luminosities $\sim 10^{44}$ erg s^{-1}: the implications of this work have been described elsewhere.

Key words: catalogues – surveys – galaxies: clusters: general – X-rays: galaxies: clusters.

1 INTRODUCTION

Part of the standard model of modern cosmology is that the structures observable in the local universe formed by gravitational instability from small fluctuations in the initial density field. As these fluctuations have now been observed (e.g. Smoot et al. 1992; Bennett et al. 1996), there has been much interest in using observations of the Universe at different look-back times to place constraints on popular models of structure formation. Cosmologists therefore need objects for which the measurable properties can be simply related to the underlying mass distribution and that are observable from the local Universe out to high redshift.

Clusters of galaxies form one such class, and have a long history of use as cosmological probes. Their importance to modern cosmology is twofold: first, they are the largest objects in the Universe that are close to virial equilibrium, and so their properties are assumed to be shaped primarily by gravity; secondly, they correspond to high peaks in the initial density field, and so their abundance is sensitive to the power spectrum of these fluctuations. Clusters therefore provide a means of comparing theory to observation: for instance, the distribution of mass on large scales (e.g. Bahcall & Soneira 1983; Kaiser 1984; Peacock & West 1992; Romer et al. 1994; Nichol, Briel & Henry 1994; Collins et al. 2000) or the evolution of this mass field (e.g. Kaiser 1986; Edge et al. 1990; Henry & Arnaud 1991; Eke, Cole & Frenk 1996; Reichart et al. 1999). This second topic is of particular interest since the growth of mass fluctuations on cluster scales is strongly dependent on the total mass content of the Universe, with only a mild sensitivity to either the cosmological constant or the slope of the power spectrum on cluster scales (e.g. Eke et al. 1996).

One of the primary motivations behind searches for clusters over the past 15 years has been the issue of evolution, namely how does the number density of clusters change with lookback time. Rather than search for clusters as peaks in the projected galaxy distribution at optical wavelengths, most of the recent work has been directed towards detecting the emission from the dominant baryonic component of clusters, the intracluster medium (ICM), which comprises around 15 per cent of the total cluster mass (Evrard 1997; Ettori & Fabian 1999; Mohr, Mathiesen & Evrard 1999; Grego et al. 2001). This hot (10^7–10^8 K), diffuse plasma emits at X-ray wavelengths via thermal bremsstrahlung (Sarazin 1988), with the result that clusters are amongst the most luminous objects in the X-ray sky, having bolometric luminosities in the range $\sim 10^{43-46}$ erg s^{-1}.

There are two main reasons for using X-ray data to select cluster samples. First, X-ray selection is free from projection effects – namely the inclusion of spurious sources due to the projection of unrelated systems along the line of sight (e.g. Frenk et al. 1990; Reblinsky & Bartelmann 1999) – because the emission is centrally concentrated (it scales as the square of the ICM density, Sarazin 1988), and it indicates the presence of an actual physical object, namely the gas trapped in the potential well of the cluster. Secondly,

⋆E-mail: dburke@cfa.harvard.edu

the measurable X-ray parameters – luminosity (L_x) and temperature (T_x) – are closely related to the mass of the cluster (e.g. Frenk et al. 1990; van Haarlem, Frenk & White 1997).

The *HEAO*-1 A-2 experiment produced the first X-ray-selected cluster sample (Piccinotti et al. 1982). This consisted of 30 clusters, with $z \lesssim 0.1$, detected over an area corresponding to 66 per cent of the sky. Edge et al. (1990) extended this sample with the *Ariel V* all-sky survey, using observations by *EXOSAT* and *EINSTEIN* to reduce confusion effects. The resulting catalogue consists of 46 clusters with fluxes greater than 1.7×10^{-11} erg cm^{-2} s^{-1} in the 2–10 keV passband. The slope of the number–flux relation for luminous clusters, with $L > 8 \times 10^{44}$ erg s^{-1}, differs from that of the low-luminosity sample, with too few luminous clusters detected at faint fluxes. This was interpreted as strong negative evolution of bright clusters at $z \sim 0.1$. David et al. (1993) also found evidence for low-redshift evolution of the most luminous clusters using essentially the same sample.

The *EINSTEIN* Extended Medium Sensitivity Survey (EMSS; Gioia et al. 1990) also produced evidence for negative evolution in the cluster population. The EMSS consists of sources detected serendipitously in *EINSTEIN* observations; although the area covered is smaller than the Edge et al. (1990) survey, the flux limit is approximately 100 times fainter, and in a softer passband (0.3–3.5 keV). The latest version of the catalogue (Gioia & Luppino 1994) consists of 104 clusters with redshifts less than 0.9. Since the survey is constructed from serendipitous observations, the flux limit is a function of sky coverage, with the faintest limit being 1.3×10^{-13} erg cm^{-2} s^{-1} over an area of 40 deg^2. Henry et al. (1992) compare the X-ray luminosity function (XLF) of clusters in different redshift shells and find a significantly steeper slope at $z = 0.33$ than at $z = 0.17$, concluding that there are fewer high-luminosity clusters at high redshift than at present.

These observational results can be tested using data from *ROSAT*, in particular from the Position Sensitive Proportional Counter (PSPC), which is roughly three times more sensitive and has twice the spatial resolution of the *EINSTEIN* IPC used by the EMSS. Cluster surveys using the *ROSAT* All-Sky Survey (RASS) data have provided a comprehensive census of the local ($z \lesssim 0.3$) cluster population (e.g. Ebeling et al. 1996, 1997; de Grandi et al. 1999a; Böhringer et al. 2000; Ebeling et al. 2000). The local XLF is constructed from samples containing $\sim$ 200–450 clusters apiece, is known over two decades in L_x, covering a factor of $\sim 10^5$ in space density, is well fitted by a Schechter function (Ebeling et al. 1997; de Grandi et al. 1999b) and shows that the evolution seen in the samples of Edge et al. (1990) and David et al. (1993) is due to local inhomogeneities in the density field of clusters at $z \approx 0.1$ (Ebeling et al. 1997). There is therefore little, if any, evolution in the space density of clusters out to $z \sim 0.3$.

The pointed phase of *ROSAT* observations produced a large data base of deep pointings, which have been used to study the cluster population out to $z \approx 1$. Cluster surveys using this data base cover a much smaller area than the RASS, and so are not sensitive to the most luminous, and hence rare, clusters; however, they are able to detect the much more numerous population of clusters with luminosities $\sim 10^{44}$ erg s^{-1}. This paper presents the catalogue of one such survey – the Southern Serendipitous High-redshift Archival *ROSAT* Cluster (SHARC) survey – which is a deep, small-area survey designed to study the high-redshift cluster population. This survey is complemented by the Bright SHARC catalogue (Romer et al. 2000), which has a flux limit $\sim$3 times higher than the Southern SHARC catalogue while covering 10 times the survey area.

The first look at the $z > 0.3$ *ROSAT*-selected cluster population was by the *ROSAT* International X-ray and Optical Survey (RIXOS). Castander et al. (1995) claimed strong negative evolution at fainter luminosities than are seen in the EMSS, since their number–redshift distribution, $N(z)$, did not match the no-evolution predictions. However, Collins et al. (1997), using the same technique, showed that the $N(z)$ distribution of the Southern SHARC survey was consistent with no evolution in the XLF and Mason et al. (2000) have now concluded that the evolution seen in the RIXOS sample is an artefact of their source-detection strategy. Nichol et al. (1997) used *ROSAT* data to reanalyse the EMSS sample, concluding that the evidence for evolution was no longer statistically significant. Both Ellis & Jones (2002) and Lewis et al. (2002) have revisited the EMSS cluster catalogue – using *ROSAT* and *EINSTEIN* data, respectively – and come to similar conclusions to Nichol et al. (1997).

Independent confirmation of little, or no, evolution – at least for moderate luminosity clusters ($\lesssim 2 \times 10^{44}$ erg s^{-1}) out to $z \sim 0.5$ – has now been provided by a number of surveys: the *ROSAT* Distant Cluster Survey (RDCS) used the number count–flux distribution [$N(S)$; Rosati et al. 1995] and later the XLF (Rosati et al. 2000); the Southern SHARC used the $N(z)$ (Collins et al. 1997) and the XLF (Burke et al. 1997); the Wide-Angled *ROSAT* Pointed Survey (WARPS-I) used the $N(S)$ distribution (Jones et al. 1998); the Bright SHARC used the XLF (Nichol et al. 1999; Adami et al. 2000); and the 160 deg^2 *ROSAT* Survey (hereafter VMF98) used the $N(z)$ and $N(S)$ distributions (Vikhlinin et al. 1998b). Evidence for evolution has been found at the bright end of the XLF (Ebeling, Edge & Henry 2000; Moretti et al. 2001; Henry 2002).

This paper presents the Southern SHARC catalogue. Section 2 describes the creation of the X-ray-selected sample from *ROSAT* PSPC data, and Section 3 describes the optical identification programme and presents the cluster catalogue. The cosmological implications of this survey have been described in Collins et al. (1997) and Burke et al. (1997). A flat cosmological model with $\Omega_\Lambda = 0$ and $H_0 = 50$ km^{-1} s^{-1} Mpc^{-1} is assumed for this work. Unless otherwise specified, the term cluster is used throughout this paper to indicate a broad class of objects, covering fossil/isolated ellipticals (Ponman et al. 1994; Vikhlinin et al. 1999; Romer et al. 2000) and poor groups up to rich clusters.

2 CONSTRUCTING THE X-RAY CLUSTER SAMPLE

Sections 2.1 and 2.2 discuss instrument and source characteristics that impact upon a search for clusters in *ROSAT* data. These are followed by a discussion of the fields selected for the survey (Section 2.3) and the steps taken to analyse each field (Section 2.4). The properties of the full source catalogue – both point-like and extended – are examined in Section 2.5. The discussion of the creation of the source sample concludes by a description of survey selection function calculations (Section 2.6) and results (Section 2.7).

2.1 Instrument details

ROSAT (Briel et al. 1994) carried two instruments capable of detecting clusters, the High Resolution Imager (HRI) and the PSPC [the strong absorption at ultraviolet (UV) wavelengths by the interstellar medium of the Galaxy means that cluster surveys are not possible with the third instrument on board *ROSAT*, the Wide-Field Camera]. Although the HRI has approximately five times better spatial resolution than the PSPC, its poorer sensitivity (approximately one-third that of the PSPC) and much higher background rate (approximately 10 times that of the PSPC) make it less attractive for faint

cluster surveys. The Southern SHARC survey is therefore restricted to PSPC data.

As its name suggests, the PSPC uses proportional counters to detect incoming photons, and so has moderate spectral and spatial resolution. The energy resolution is $\Delta E/E = 0.43\ (E/0.93)^{-1/2}$ across the detector, with E measured in keV. On-axis, the point spread function (PSF) has a full-width half-maximum (FWHM) of $\simeq$25 arcsec at 1 keV; off-axis, the FWHM is $\simeq$55 arcsec at 20 arcmin and increases rapidly at larger radii (Boese 2000). The central $\sim$20 arcmin radius of the detector is unobstructed, whilst at larger radii the support structure of the PSPC window causes strong vignetting. Therefore, to ensure the greatest sensitivity and a small PSF, the survey is limited to those areas within an 18-arcmin radius of the centre of the detector. The pixel size is chosen to be the standard value of 15×15 arcsec^2.

2.2 Search criterion

Although rich clusters are very luminous, they are rare objects; for deep *ROSAT* observations the X-ray sky is dominated not by clusters, but by active galactic nuclei (AGN) and quasi-stellar objects (QSOs) (e.g. Hasinger et al. 1998; McHardy et al. 1998). In order to produce a catalogue of cluster candidates that can be identified in a reasonable amount of optical telescope time, extra criteria must be used to efficiently select clusters. It is also important that these criteria produce a well-defined cluster sample, to allow comparison with both theory and other cluster surveys.

2.2.1 Detecting clusters

The X-ray data are used to distinguish between clusters and other sources. One possibility is to use the source spectrum, since non-cluster X-ray sources tend to have either power-law spectra (e.g. active galaxies) or thermal spectra at significantly cooler temperatures than clusters (e.g. coronal stellar emission). However, the limited spectral resolution of the PSPC precludes detailed spectral analysis (e.g. Vikhlinin et al. 1995; Almaini et al. 1996; Mittaz et al. 1999). Although the hardness ratio has been used as a crude spectral indicator (Ebeling et al. 1998), it was found to not significantly reduce the contamination rate in this survey (Section 2.5) and so was not used.

As the majority of X-ray sources are compact objects, whereas cluster emission is from a diffuse component, an obvious discriminant is the count distribution; one should select objects that are extended compared with the instrumental PSF. This requires that the PSF is both small enough, and well enough defined, to allow clusters at the redshifts of interest to be detected as extended. Section 2.6 contains detailed simulations to test these concerns, but a simple calculation suggests that the PSPC can detect clusters as extended objects out to beyond $z = 0.6$. At $z = 0.6$, a cluster with a core radius of 250 kpc – typical of low-redshift clusters (Jones & Forman 1999) – will subtend $\sim$30 arcsec, which is similar to the on-axis PSF FWHM, and have a flux of $\sim 5 \times 10^{-3}$ count s^{-1} or $\sim$50 counts for a 10-ks exposure. Although compact clusters will be missed by this technique, it produces a well-defined cluster sample for which the selection function can be calculated by simulations. The majority of *ROSAT* high-z cluster searches use some form of extent criterion as their primary selection method.

2.2.2 Energy band

The first choice to make, when analysing *ROSAT* PSPC data, is which energy band to use since, despite the limited spectral resolution, it is possible to define several independent passbands (e.g. Snowden et al. 1994). The choice depends upon the source and background spectra; it is a trade-off between maximizing the source counts, whilst minimizing the background signal. The PSPC has three background components (Snowden et al. 1994): charged particles from the local environment, scattered solar radiation and the diffuse celestial X-ray background. Whilst the particle background spectrum is roughly independent of energy, the majority of the flux from both the celestial background and scattered solar radiation is at energies below 0.5 keV.

The XRT had little effective area above 2.0 keV, and so the energy range for the survey was chosen to be 0.5–2.0 keV, which is similar to that used in the other distant *ROSAT* cluster surveys. Since the survey is restricted to fields with a high galactic latitude ($|b^{\rm II}| > 20^\circ$), the severe absorption of the soft X-ray flux by the cool neutral gas in the Galaxy is restricted to energies below $\sim$0.5 keV – it is only when the line-of-sight column density of neutral hydrogen, $n_{\rm H}$, reaches values of 10^{21} cm^{-2} that the absorption significantly affects spectra at energies close to 1.0 keV (e.g. Brown & Gould 1970).

2.2.3 Detection method

There is currently no consensus as to the best way of detecting extended sources in X-ray data, and a variety of techniques have been employed by the *ROSAT* surveys: RIXOS uses a sliding-box technique (Mason et al. 2000); the RDCS, VMF98, BMW and Bright SHARC surveys use wavelet-based techniques (Rosati et al. 1995; Vikhlinin et al. 1998a; Lazzati et al. 1999; Romer et al. 2000); and WARPS use the Voronoi tessellation combined with a percolation (VTP) algorithm (Scharf et al. 1997). The publication of the cluster samples from the surveys listed above, combined with this survey, should eventually enable the relative merits of the techniques to be assessed. However, as discussed in Section 5, the consistency in results between the majority of the surveys suggests that there are no large-scale differences, although a detailed study is required for specific cases, such as the influence of cooling flows on cluster detectability (e.g. Pesce et al. 1990).

The method used to detect candidates for the Southern SHARC catalogue is based upon the sliding-box technique as implemented by the PSS program from the Starlink X-ray reduction package ASTERIX (Allan & Vallance 1995). There are three main differences with respect to the early sliding-box search methods (e.g. Gioia et al. 1990; Cruddace et al. 1991): the background is estimated from the whole field rather than from the edges of the detection aperture; a maximum-likelihood ratio technique assuming Poisson fluctuations (Cash 1979), rather than Gaussian, is used; and the data are compared with a model profile of the PSF to assess the significance of any possible source. The change in background subtraction reduces the chance of missing extended sources because they artificially increase the background estimate. The use of the Cash statistic is necessitated by the low background count rates measured by the PSPC: for an exposure time of 10 ks, the typical background is only 0.1–0.5 counts per 15×15 arcsec^2 pixel.

Once a source has been detected it is evaluated for extent. The PSF model is convolved with a Gaussian profile and the resulting template is used by PSS to fit the count distribution and the resulting detection significance (S, calculated using the Cash statistic) is recorded. The process is repeated for a range of Gaussian FWHM between 0 and 8 arcmin. For those FWHM values where the detection significance is greater than the PSF-only case (i.e. FWHM = 0), the change in S is used to calculate the extent significance ($S_{\rm ext}$) of

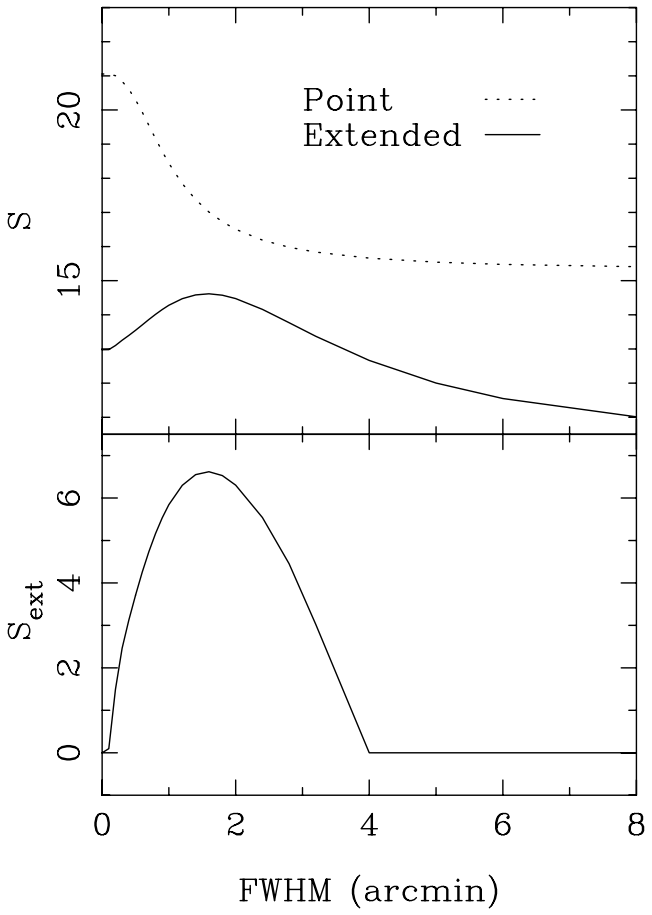

Figure 1. Variation in detection significance (S, top plot) and significance of extent (S_{ext}, bottom plot) with the size of the template used to fit the data. The template was created by convolving the model PSPC PSF with a Gaussian profile of the indicated FWHM. The two curves show typical results for a point (dotted line) and extended (solid line) source; since the point source has $S_{ext} = 0$ for all FWHM it has been excluded from the bottom plot.

the source using the maximum-likelihood ratio test (e.g. Cash 1979; Vikhlinin et al. 1998a). The extent significance for each source is then taken to be the peak value of its S_{ext} curve. Fig. 1 shows the results for a point source and a cluster (RX J1354.2–0222) detected in the survey: the top and bottom plots show how the detection significance and extent significance, respectively, vary with the profile extent.

2.3 Survey fields

The survey consists of 66 fields chosen from the publically available *ROSAT* archive in 1997, which satisfy the following criteria: cleaned exposure times greater than, or equal to, 10 ks; a Galactic latitude such that fields are more than 20° away from the Galactic plane; did not contain extended X-ray or optical emission over a significant fraction of the field; and have a declination less than +20° and right ascension outside the range 0–3 h. The exposure-time limit ensures that the observations are deep enough to detect moderate luminosity ($L_x \gtrsim 10^{44}$ erg s^{-1}) clusters at redshifts greater than 0.3, whilst the latitude limit ensures that Galactic absorption is not too high, and that the surface density of stars is not so large as to hinder optical cluster identification. The right ascension and declination limits were governed by observing constraints. The fields are listed in Table A1 and plotted on an Aitoff projection of the sky in Fig. 2. Fig. 3 shows the distribution in exposure time and Galactic hydrogen column density (taken from Marshall & Clark 1984) of these fields; the median values are 15 ks and 3.5×10^{20} cm^{-2}, respectively. Of these fields, 61 are also in the Bright SHARC survey, 28 in the survey of VMF98 and seven in the WARPS-I survey, as indicated in Table A1. Although the same fields are used, the surveys use different search algorithms, reach different flux limits, and use different regions of each field (Section 4).

The catalogue is restricted to those sources for which the centres lie within 18 arcmin of the field centre. Also excluded are regions surrounding the target of the observation. In the vast majority of cases, the target could be identified from the observation name and the masking radius was determined by examining the X-ray and optical data for these sources, using a minimum value of 3 arcmin and a maximum value of 8.4 arcmin; for the majority of sources a radius of 5 arcmin was used. Three fields had two sources that required masking and there were nine fields for which the whole image could be used because the target lay outside the central region. For the two fields in which the target could not be identified, a fiducial radius of 5 arcmin was used, placed at the centre of the field. Observations that targeted clusters were included in the survey as long as the X-ray emission did not extend beyond a radius of 10 arcmin. The masked regions, which are listed in Table A1, only account for 5 per cent of the total survey area of 17.7 deg^2.

2.4 Data reduction

The data reduction consists of filtering the data to remove unwanted data, estimating the background, and then source detection. These steps are described in more detail below.

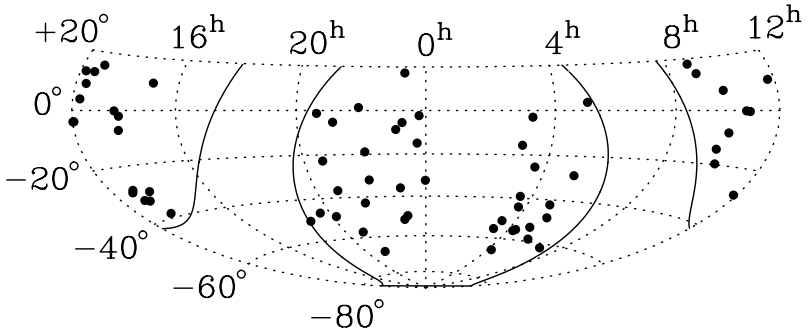

Figure 2. Distribution on the sky – using an Aitoff projection in equatorial coordinates – of the fields used in the survey. The solid lines indicate the Galactic latitude limit ($|b^{II}| > 20°$), and the gap between 0 and 3 h was due to observing constraints.

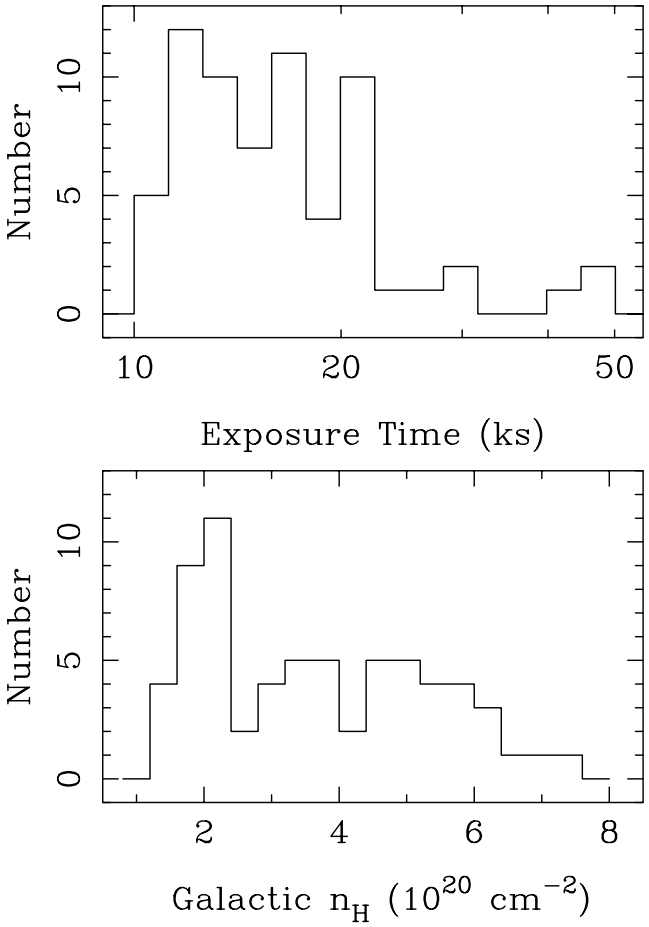

Figure 3. Distribution of the exposure times (after cleaning) and Galactic n_H values for the fields used in the survey. The median values are 15 ks and 3.5×10^{20} cm^{-2}, respectively.

2.4.1 *Data filtering*

The first step in reducing PSPC data is to select those periods of the observation that contain scientifically useful data. Two filters were applied: first, to ensure that the model used to calculate the background components is valid, the master veto rate – a measure of the particle background – had to be less than 170 (Snowden et al. 1994) and secondly that periods during which the aspect solution was poor were rejected, since the distinction between point and resolved sources is of vital importance. The rejected periods were mainly small, around 5 per cent, with a maximum reduction of 20 per cent; those observations for which this cleaned observation time fell below 10 ks were removed from the sample.

2.4.2 *Estimating the background*

The source detection routine requires knowledge of the background for each pixel of the field, which was estimated from an image of the field in which the sources had been masked out. The method used to create this masked image is to assume that the background can be approximated by a single value – the initial background estimate – and then run PSS on the field. The detected sources are masked from the field, and the resulting image used to calculate the model background for the field.

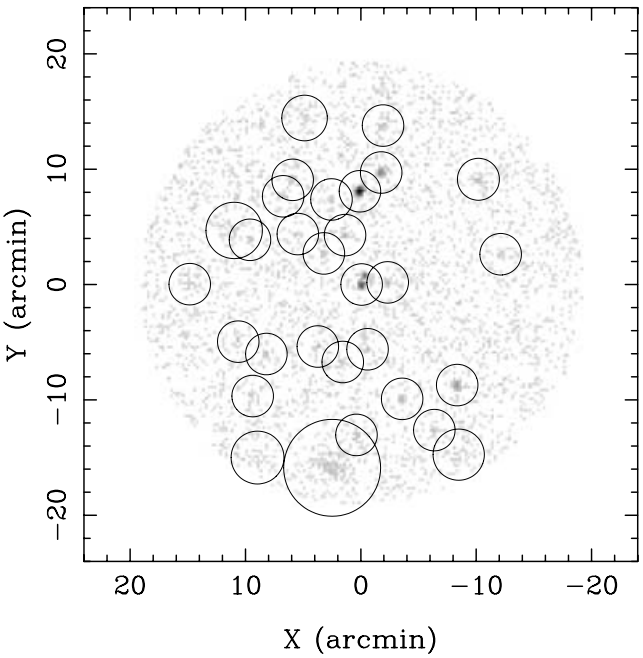

Figure 4. Central region (19.2-arcmin radius) of a PSPC field used in the survey. The circles indicate the regions removed from the background calculation (which accounts for ∼30 per cent of the area). In order to highlight the range of source fluxes, a square-root scaling has been used.

As the background count rates are low, both the median and mode of the fields used in the sample are zero, so the initial background estimate is calculated using a sigma-clipped mean. PSS is then run on the field, detecting sources above a 4σ threshold. The blanking radius to use for each source is defined as the 99.7 per cent radius (3σ) of the best-fitting Gaussian to the source radial profile. This radius was chosen as a compromise between removing a high percentage of the source counts and ensuring enough of the field is left to calculate the model background. Fig. 4 shows the masked regions for one of the fields in the survey; the masking removed 29 per cent of the field area. Fig. 5 shows how the radial profile of the field is changed by the background masking, and how it compares with the model background.

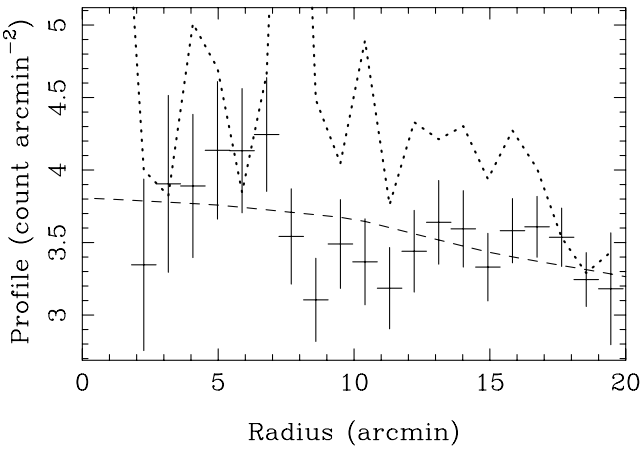

Figure 5. Radial profile of the field shown in Fig. 4 before (dotted line) and after (crosses) masking out the detected sources. The dashed line indicates the radial profile of the model fit to the masked data.

2.4.3 *Source detection*

The source detection has been implemented as a two-stage process: the first stage involves running the detection algorithm on the field to produce a source list (the first-pass source list), in the second stage each source is examined to see whether the count distribution is extended (the second-pass source list). Since the first-pass detection routine uses an aperture optimized for detecting point sources, a 4σ threshold is used, rather than the more-conservative 5σ limit used in the second pass. This reduced limit is a compromise between ensuring extended low surface-brightness sources are not missed and reducing the contamination rate of spurious sources associated with background fluctuations.

For each source in the second-pass list the extent significance is calculated as described in Section 2.2.3. The hardness ratio of each source is calculated by

$$\mathrm{HR} = \frac{\mathrm{hard} - \mathrm{soft}}{\mathrm{hard} + \mathrm{soft}}, \quad (1)$$

where 'soft' and 'hard' refer to the source counts in the 0.11–0.5 and 0.5–2.0 keV bands, respectively. Although the detection procedure uses the data out to a radius of 19.2 arcmin, only those sources with centres which lie within 18 arcmin of the detector centre are included in the source list, in order to reduce edge effects. The final catalogue consists of those sources that are detected at 5σ or better in the second-pass list and for which the extent significances are greater than, or equal to, 3σ.

2.5 Detected sources

The full catalogue consists of 1521 sources, 96 (6 per cent) of which are flagged as extended by the source-detection algorithm; the identification of the extended sources is discussed in Section 3.1. As fluxes were not calculated for the point sources, it is not possible to compare the $\log N - \log S$ distribution with those from other deep PSPC surveys. However, the average surface density of all sources in this survey, 86 deg^{-2}, corresponds to a flux density of $\sim 1 \times 10^{-14}$ erg cm^{-2} s^{-1} (e.g. Georgantopoulos et al. 1996). As this is approximately the flux limit that the survey is expected to reach, it suggests that the detection procedure produces results similar to those of other deep PSPC surveys.

Fig. 6 shows the hardness ratio, defined using equation (1), plotted against extent significance for each source. Two reasons why the values are biased high are that the source selection is done in the hard band, and that the extraction region used to measure the flux is based on the hard-band data and the PSPC PSF is larger at softer energies (Boese 2000). Whilst this a posteriori analysis does show that the clusters are hard, as expected (e.g. Ebeling et al. 1998), it also shows that the use of the hardness ratio does not significantly improve the efficiency of the selection process for this sample.

2.6 Simulations

The selection function of the Southern SHARC survey was calculated using a Monte Carlo method to generate simulated cluster images. The ability to detect a given cluster depends on properties both intrinsic and extrinsic to it. The relevant cluster characteristics are its luminosity, surface brightness profile and redshift, while those for the survey are the exposure time, the background count rate and the off-axis angle. Since the distribution of cluster profiles is not known a priori, a profile similar to that derived from local samples was used, namely a King profile – $S_0(r) \propto [1 + (r/r_c)^2]^{0.5-3\beta}$ – with β set to $\frac{2}{3}$ and a wide range of core radii (Henry et al. 1992; Jones & Forman 1999; Vikhlinin, Forman & Jones 1999). Vikhlinin et al. (1998b) find little evidence for evolution in the core radius from the nominal value of $\sim$250 kpc out to $z \sim 0.5$, although they studied more luminous clusters than are discussed here.

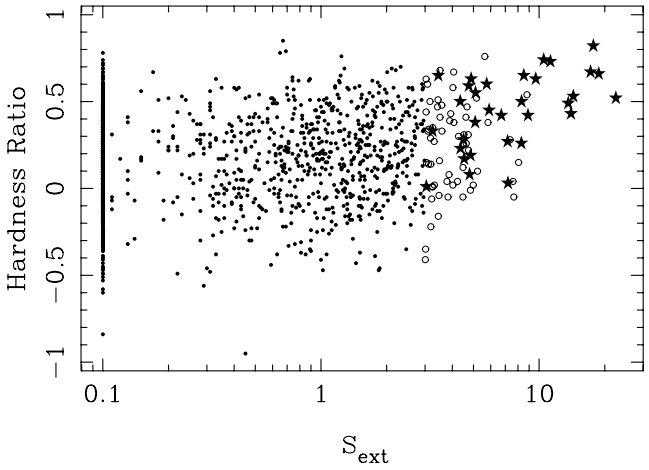

Figure 6. Hardness ratio and significance of extent ($S_{\rm ext}$) for the sources detected in this survey: for display purposes all sources with $S_{\rm ext} < 0.1$ have been set to 0.1. Clusters are labelled using a filled star, other extended sources are labelled with an open circle, and all other points are labelled with a filled circle.

A 6-keV thermal bremsstrahlung model was used to convert between cluster count rates and fluxes, as well as to calculate the k-correction between observed and rest-frame passbands. Galactic absorption was calculated using a column density corresponding to the median survey value ($n_{\rm H} = 3.5 \times 10^{20}$ cm^{-2}, Section 2.3) and the cross-sections from Morrison & McCammon (1983). The conversion factor between the count rate and the luminosity varies by $\lesssim$5 per cent for plasma temperatures typical of high-redshift clusters with 0.5–2.0 keV luminosities $\sim 10^{44}$ erg s^{-1} (Fairley et al. 2000).

2.7 Simulation results

Fig. 7 shows the results of the simulations following the presentation used by Scharf et al. (1997), where the contours indicate the available

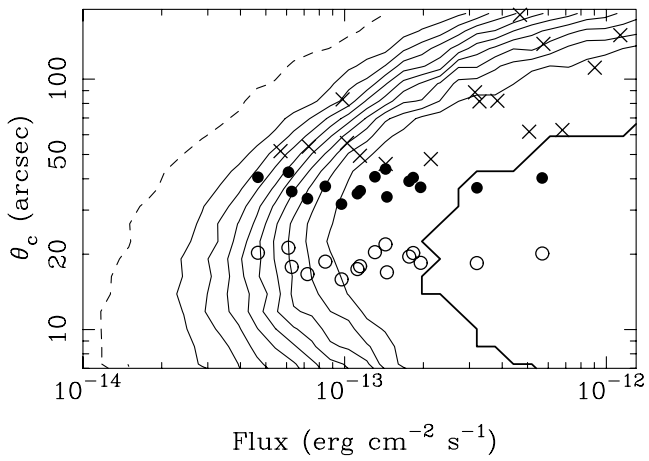

Figure 7. Survey area, as a function of cluster flux and core radius, following fig. 8 of Scharf et al. (1997). The dashed line represents 1 per cent of the survey area, with the solid lines indicating the 10–100 per cent contours (the thick solid line corresponds to the 100 per cent value). Also shown, as solid circles and crosses, respectively, are the $z \geqslant 0.3$ and $z < 0.3$ subsamples of the Southern SHARC catalogue. The open circles show the position of the high-z subsample if the core radius were 125 kpc.

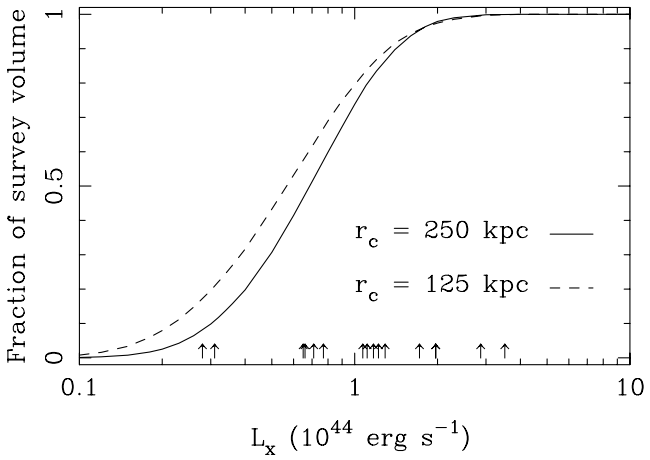

Figure 8. Survey volume, $V_{\max}(L_x)$, for the redshift shell $z = 0.3$–0.7, for a range of cluster luminosities. The curves were calculated using equation (2) and the selection function presented in Fig. 7, assuming that the core radius of all clusters is either 250 kpc (solid line) or 125 kpc (dashed line), and is independent of redshift. The arrows indicate the luminosities of the Southern SHARC sample for this redshift shell.

survey area for a cluster of a given flux and core radius. The influence of the extent criterion used in the detection procedure is evident as the decrease in detection efficiency at small θ_c. Also shown (as the solid circles and crosses) are the 32 clusters in the Southern SHARC catalogue, where the θ_c values have been calculated assuming a core radius of 250 kpc. 70 per cent of the $z \geqslant 0.3$ sample are visible over 90 per cent of the survey area.

For a given cosmological model, it is easier to visualize the selection function using the approach of Burke et al. (1997), who presented the survey volume in a fixed redshift shell as a function of cluster luminosity, $V_{\max}(L_x)$. Defining $\Omega(z, L_x)$ as the survey area of a cluster at a redshift z and luminosity L_x, then

$$V_{\max}(L_x) = \int_{z_1}^{z_2} \Omega(z, L_x)\, \mathrm{d}V(z)\, \mathrm{d}z, \qquad (2)$$

where d $V(z)$ is the volume per unit area at a redshift z and a single core radius has been assumed. The $V_{\max}$ curve is shown in Fig. 8 for the redshift shell $z = 0.3$–0.7, with $r_c = 250$ kpc, and indicates that the minimum detectable luminosity is approximately 3×10^{43} erg s^{-1}, while clusters with luminosities of 3×10^{44} erg s^{-1} are observable out to beyond $z = 0.7$. As the volume of this shell is close to 4×10^7 Mpc^3, the survey is unlikely to detect high-redshift clusters with space densities below 10^{-8} Mpc^{-3}. This corresponds to a maximum detectable luminosity of $\sim 4 \times 10^{44}$ erg s^{-1} using the XLF of Ebeling et al. (1997) and assuming no positive evolution in the XLF.

If there is evolution of, or correlations between, parameters of the cluster profile (e.g. if the core radius changes with redshift or luminosity), then the selection function will be biased and care must be taken in interpreting calculations that use this data. The cluster-evolution model of Bower (1997) predicts a decrease in core radius by no more than 50 per cent out to $z \simeq 0.5$ for a reasonable range of model parameters. The open circles in Fig. 7 and the dashed line in Fig. 8 represent the extreme version of such a model, in which all $z > 0.3$ clusters have a core radius of 125 kpc. The results are not significantly different, with the maximum increase in survey volume being a factor of 2 for the two clusters with luminosities $\sim 3 \times 10^{43}$ erg s^{-1}. However, as previously discussed in Section 2.6, the empirical evidence is of little, if any, evolution of the core radius out to $z \sim 0.5$ (Vikhlinin et al. 1998b).

3 THE CLUSTER CATALOGUE

The identification of the extended sources in the Southern SHARC catalogue – both from the literature and via optical follow-up work – is discussed in Section 3.1. The calculation of the cluster X-ray fluxes and luminosities is described in Section 3.2 and listed in Table 1.

3.1 Identification of extended X-ray sources

A literature search – using the NASA Extragalactic Database (NED) – was made to find those extended X-ray sources that were already identified. Further identification was made using contour plots of the X-ray emission overlaid on digitized images from the Palomar and UK Schmidt Sky Survey plates. In addition to several nearby galaxies, several sources were found to be identified with stellar-like objects; these were identified as extended either due to contamination by a nearby source, or because the source was so bright that the count statistics were good enough that the differences between the model and real PSF became significant. The remaining sources were identified using a combination of R-band imaging ($R \sim 23$ in 1-arcsec seeing) and medium-resolution optical spectroscopy.

The use of a red filter for the imaging observations enhances the contrast of clusters over the background population, since the central regions of clusters are dominated by old, red elliptical galaxies (e.g. Bower, Lucey & Ellis 1992; Aragón-Salamanca et al. 1993; Stanford, Eisenhardt & Dickinson 1998) and the field galaxy population becomes bluer at fainter magnitudes (e.g. Smail et al. 1995; Hogg et al. 1997). Those sources that showed an overdensity of galaxies, as estimated by eye, close to the X-ray centroid were selected for spectroscopic identification. Spectra were obtained for galaxies and point sources close to the X-ray centroid, using a single slit or a multi-object mask where appropriate. The aim was to obtain a minimum of three concordant redshifts per cluster; the size of the field available for spectroscopy meant that the number of objects observed per source was typically between two and 10.

The fields were all imaged using the EFOSC-I instrument on the ESO 3.6-m telescope. This instrument was also used to obtain spectroscopic identification of targets using both its single-slit and multi-object modes. Additional multi-object spectroscopy was obtained using LDSS-I on the AAT and LDSS-II on the WHT, with one additional identification (RX J1313.6–3251) provided by H. Ebeling using the University of Hawaii 2.2-m telescope. The spectral resolution of the observations was ≈10–20 Å, typically covering 3800–7500 Å, sufficient to identify cluster galaxies from their absorption-line features out to redshifts of at least 0.7.

The optical data were reduced using standard procedures provided by the STARLINK software packages. After bias subtraction and flat-fielding, individual exposures were combined – shifts due to flexure were less than a pixel – and cosmic ray events removed from the data. Spatial profiles of the emission from each slit were used to identify regions of source and sky emission. The same regions were used to calculate the wavelength calibration; use of third- or fourth-order polynomials resulted in residuals of ∼0.3 Å. The resulting background-subtracted spectra typically had continuum signal-to-noise ratios of ∼10 per resolution element.

Identification of the spectra was performed manually: the most common features seen in galaxies were – in absorption – the Ca II, H and K doublet, 4000-Å break, the G band and the Balmer series,

Table 1. The Southern SHARC catalogue.

Name	ROR	θ	z	r_{80}	Area	$n_{\rm ph}$	$c_{\rm tot}$	$n_{\rm H}$	f_{14}	$\delta L/L$	$L_{\rm R}$	$L_{\rm E}$	QF	N
RX J0318.2–0301	800555	6.9	0.370	3.30	74	120.5	0.0136	5.67	18.28	0.104	1.11	1.99	1	1
RX J0318.5–0303	800555	10.5	0.373	3.29	86	364.0	0.0424	5.67	56.86	0.072	3.51	6.31	1	2
RX J0333.0–3914	800367	7.4	0.245	4.21	95	42.5	0.0047	2.33	5.69	0.161	0.15	0.27	2	–
RX J0334.0–3901	800367	14.0	0.064	12.23	60	664.3	0.0926	2.33	113.12	0.063	0.20	0.36	1	3
RX J0337.7–2522	300079	2.7	0.577	2.72	83	213.0	0.0060	1.57	7.21	0.085	1.07	1.93	1	4
RX J0416.7–5525	600623	16.2	0.365	3.33	73	100.7	0.0107	2.07	13.06	0.112	0.77	1.39	1	–
RX J0505.3–2849	700233	15.2	0.509	2.85	86	101.0	0.0093	1.73	11.19	0.111	1.29	2.32	1	–
RX J0505.9–2826	700233	9.6	0.131	6.65	77	325.1	0.0273	1.73	32.76	0.075	0.25	0.44	1	5
RX J0530.5–5852	300130	8.6	0.338	3.47	100	23.5	0.0049	3.26	6.10	0.212	0.31	0.55	3	–
RX J0858.4+1357	700436	12.3	0.485	2.91	98	66.1	0.0048	4.26	6.28	0.133	0.66	1.18	1	6
RX J0946.5–1410	701458	15.6	0.230	4.39	64	56.6	0.0055	5.23	7.30	0.142	0.17	0.31	1	–
RX J0947.9+0730	701587	6.0	0.128	6.78	88	30.3	0.0077	4.02	9.82	0.188	0.07	0.13	2	–
RX J1142.0+1009	600420	8.1	0.118	7.24	83	202.0	0.0262	1.80	31.50	0.086	0.19	0.34	1	7
RX J1142.2+1027	600420	10.2	0.070	11.29	83	359.1	0.0478	1.80	57.51	0.073	0.12	0.22	1	8
RX J1200.8–0328	701202	14.5	0.395	3.19	95	122.1	0.0140	3.38	17.64	0.103	1.22	2.20	1	9
RX J1204.3–0351	201367	10.7	0.262	4.03	85	187.9	0.0091	3.51	11.44	0.088	0.35	0.62	1	10
RX J1205.0–0333	201367	12.1	0.368	3.31	96	77.3	0.0037	3.51	4.66	0.124	0.28	0.50	1	11
RX J1227.2+0858	600587	11.7	0.090	9.07	70	761.2	0.0752	1.75	90.36	0.062	0.32	0.57	1	12
RX J1253.2+1556	800393	14.0	0.275	3.91	94	141.9	0.0176	2.07	21.36	0.098	0.71	1.28	1	13
RX J1313.6–3251	300219	9.9	0.052	14.76	70	326.8	0.0356	5.07	46.78	0.075	0.05	0.10	1	14
RX J1325.0–3814	600419	11.5	0.296	3.74	91	133.9	0.0108	5.33	14.35	0.100	0.56	1.00	1	15
RX J1325.5–3826	600419	3.3	0.445	3.02	93	212.7	0.0146	5.33	19.52	0.085	1.72	3.09	1	16
RX J1338.0–2944	600188	16.2	0.189	5.03	83	557.1	0.0390	4.69	50.73	0.066	0.80	1.43	1	17
RX J1354.2–0222	701500	16.0	0.551	2.76	93	96.1	0.0113	3.99	14.51	0.114	1.97	3.53	1	18
RX J2038.4–0125	300218	5.8	0.673	2.59	94	104.7	0.0071	5.98	9.73	0.110	1.97	3.55	1	19
RX J2106.8–0510	300389	17.6	0.449	3.01	79	431.8	0.0242	5.00	32.02	0.069	2.87	5.16	1	–
RX J2108.8–0517	300389	13.5	0.320	3.58	86	196.7	0.0109	5.00	14.33	0.087	0.65	1.17	1	20
RX J2114.3–6801	900133	13.7	0.130	6.69	83	442.8	0.0308	3.03	38.35	0.069	0.28	0.51	1	21
RX J2137.8–4251	800336	14.3	0.185	5.11	76	417.5	0.0559	2.22	67.94	0.070	1.02	1.83	1	22
RX J2155.9+0109	800344	10.9	0.219	4.54	83	64.3	0.0078	4.65	10.21	0.134	0.22	0.39	2	–
RX J2202.7–1902	700516	8.3	0.436	3.05	93	110.2	0.0068	2.69	8.44	0.108	0.71	1.28	1	23
RX J2359.5–3211	800372	7.5	0.478	2.92	100	113.7	0.0095	1.56	11.46	0.106	1.17	2.10	1	24

X-ray fluxes and luminosities of the clusters listed in order of ascending right ascension (the coordinates of the clusters are given in Table B1): ROR gives the name of the field the source is detected in; θ lists the off-axis angle of the cluster in arcmin; z is the cluster redshift; r_{80} gives the radius (in arcmin) of the aperture used to measure the count rate; Area gives the percentage of the aperture that remained after masking out contaminating sources; $n_{\rm ph}$ is the number of source counts within this aperture; $c_{\rm tot}$ gives the total cluster count rate in count s^{-1} (this has been corrected for the signal falling outside the aperture); $n_{\rm H}$ values are in units of 10^{20} cm^{-2} and are taken from the compilation of Marshall & Clark (1984); f_{14} is the total cluster flux in units of 10^{-14} erg cm^{-2} s^{-1} for the 0.5–2.0 keV passband; and $L_{\rm R}$ and $L_{\rm E}$ give the cluster luminosity in units of 10^{44} erg s^{-1} (R indicates the 0.5–2.0 keV passband, E indicates the 0.3–3.5 keV passband). The error, $\delta L/L$, is the Poisson error on the number of source counts added, in quadrature, to a 5 per cent error to account for uncertainties due to the use of a single temperature in the flux conversion. The QF column indicates the quality flag of the cluster as discussed in Section 3.2. The final column, N, indicates those clusters that are also detected in other surveys, as listed in Table B1: 1 is BS RX J0318.2–0301; 2 is BS RX J0318.5–0302; 3 is A3135; 4 is [VMF98] 033; 5 is [VMF98] 038; 6 is [VMF98] 066 and RIXOS F250_057; 7 is A1354; 8 is A1356 and BS RX J1142.2+1026; 9 is [VMF98] 111, RIXOS F222_504 and BSe RX J1200.8-0327; 10 is [VMF98] 113 and BSe RX J1204.3-0351; 11 is BSe RX J1205.0−0332; 12 is 8 arcmin from A1541 ($z = 0.089$); 13 is BSe RX J1253.2+1556; 14 is BS RX J1313.6−3250; 15 is BSe RX J1325.0−3814; 16 is BSe RX J1325.6−3825; 17 is MS 1335.2−2928; 18 is [VMF98] 151; 19 is WARP J2038.4−0125; 20 is [VMF98] 200 and WARP J2108.8–0516; 21 is [VMF98] 201 and DS 210958–681304; 22 is A3791; 23 is [VMF98] 205; and 24 is BSe RX J2359.5–3211, 7.5 arcmin away from F1637.23TL ($z = 0.48$).

and, in emission, the [O II], [O III] and Hβ lines. Additional features seen included broad metallic absorption lines in late-type stars and the strong emission lines characteristic of AGN and QSOs. Redshift measurements were robust with respect to the choice of feature used for the identification; tests using the cross-correlation technique (e.g. Heavens 1993) showed that redshift errors were typically ± 0.005.

Table B1 lists the cluster redshifts, calculated as the average redshift of the member galaxies, along with the identifications of the non-cluster sources. Extended sources within 1 Mpc of a cluster were considered to be part of the central cluster rather than a separate entity. There are five such sources in the survey; they are identified in Table B1 by the parentheses surrounding their ID.

A number of the sources are also detected in the Bright SHARC, VMF98, WARPS-I and EMSS surveys, as indicated in Table B1. They were identified by finding objects that fell within 1 arcmin of the Southern SHARC position: RX J1313.6–3251, which is listed in the Bright SHARC catalogue as 'id pending', has now been spectroscopically identified as being a group/isolated elliptical at a redshift of 0.052 and the redshift for the cluster RX J0505.9–2826 has been taken from VMF98. Fig. 9 compares the redshift measurements for the common clusters: the sources in VMF98 with a photometric redshift are plotted with their 90 per cent error limits. The spectroscopic redshift measurements agree and the photometric estimates from VMF98 are mainly in good agreement with the measured values. Several of the extended sources in Table B1 are identified with clusters in VMF98; they were not included in the Southern SHARC sample since the follow-up work described in this section does not indicate the presence of a cluster, and these objects only have photometric redshift measurements in VMF98. Of these sources, Romer et al. (2000) has previously discussed the case of

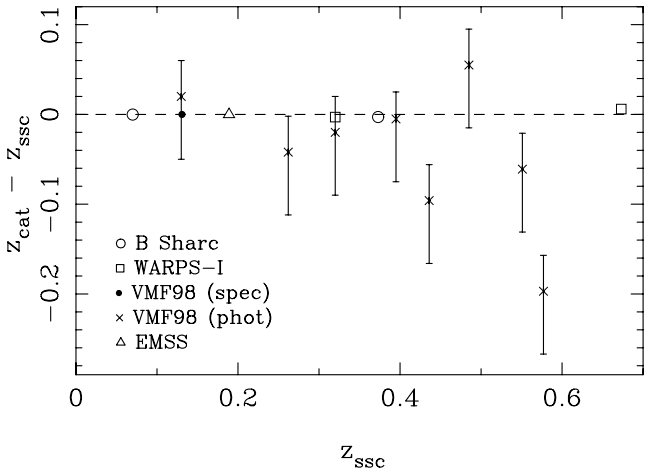

Figure 9. Comparison of the redshift measurements of the cluster catalogues, where z_{ssc} is the redshift from the Southern SHARC catalogue and z_{cat} is the redshift from one of the Bright SHARC, WARPS-I, VMF98 or EMSS catalogues. The VMF98 clusters with only photometric redshift measurements are indicated by the crosses (the error bars reflect the 90 per cent limits on z_{ph}) and the cluster with a spectroscopic redshift is labelled with a solid circle.

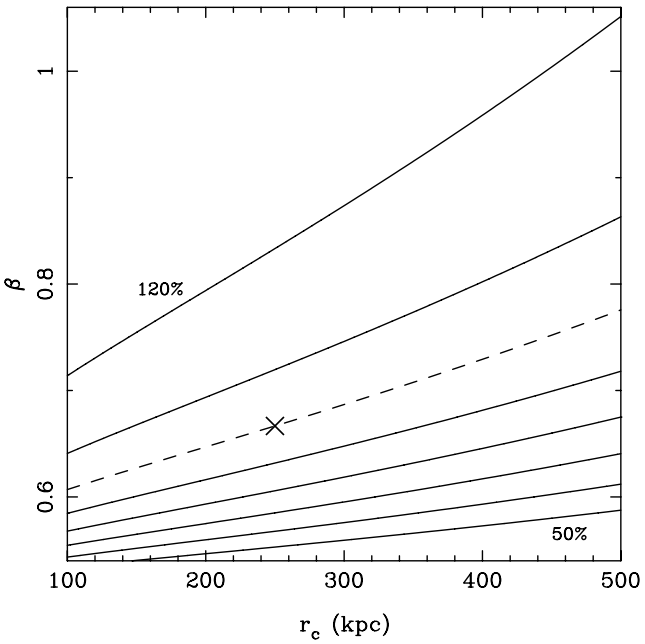

Figure 10. Measured count rate, as a percentage of the true value, if the cluster profile does not match the canonical value of $r_c = 250$ kpc and $\beta = \frac{2}{3}$ (indicated by a cross). The lines are in steps of 10 per cent, increasing from 50 per cent at the bottom of the plot to 120 per cent at the top of the plot (the dashed line corresponds to 100 per cent).

RX J0947.8 + 0741, which is identified here with a spectroscopically identified quasar at $z = 0.63$ that may be part of a cluster.

The catalogue contains 32 clusters, with redshifts between 0.05 and 0.67, 16 of which have $z \geqslant 0.3$. It is derived from an initial list of 96 extended X-ray sources, eight of which have no identification, and so the completeness rate for the survey is 92 per cent. The high-redshift sample ($z \geqslant 0.3$) is the same as used by Burke et al. (1997) and Burke (1997), and so their conclusions on the XLF are unchanged. At low redshifts ($z < 0.3$), six clusters – all but one with $z < 0.2$ – presented in Burke (1997) have been removed because their centres lie outside the survey area used here, and two systems have been added (RX J1313.6–3251 and RX J0505.9–2826).

3.2 Cluster X-ray fluxes

The X-ray count rate of each cluster was measured from the appropriate count rate image – created by dividing the image used in the cluster-detection process (Section 2.4) by the exposure map for that observation – within a circular aperture, where the radius, r_{80}, was selected so as to enclose 80 per cent of the light of a King profile with $\beta = \frac{2}{3}$ and $r_c = 250$ kpc. The 80 per cent value was chosen as a compromise between including a high fraction of the flux, whilst minimizing the contamination due to unrelated sources within the region; it has the advantage that the correction to the total count rate is insensitive to the parameters of the King profile. This is illustrated in Fig. 10, which shows the estimated count rate as a percentage of the true value for a range of King profiles: for core radii in the range 100–500 kpc, the estimated flux is insensitive to the β value as long as it is $\gtrsim$0.6. Since the aperture sizes are much larger than that of the PSF, the effect of the PSF on r_{80} is negligible (less than 2 per cent), and so was ignored.

The count rate images had their backgrounds removed by subtracting the model backgrounds created in Section 2.4.2. The count rate images themselves were also used to estimate the background rate – after being masked of all detected sources – using an annulus either centred on, or at the same off-axis angle as, the cluster. All three methods produced estimates of the source flux which differed by $\lesssim$5 per cent. The resulting background-subtracted images were then masked of all sources other than the cluster, using circular apertures with radii set to the value used in the second-pass analysis of each source (Section 2.4.3). The fraction of the cluster aperture that remained after this masking, and the measured number of source counts, are listed in Table 1; for $z > 0.3$ the median area and fractional Poisson error are 93 and 10 per cent, respectively.

A radial profile of each cluster was created, and then used to replace those pixels that were either masked due to the presence of a contaminating source or fell outside the field of view of the image. The most severe contamination occurs for RX J0318.2–0301, which has an AGN, spectroscopically identified as being at $z = 0.233$, $\sim$1 arcmin north of the cluster centre. Inspection of the resulting growth curves showed that most (28 clusters) were not significantly affected by poor background models; these clusters are given a quality flag of 1 in Table 1. The remaining four clusters were reanalysed using an interactively chosen background region centred on the cluster, with an inner radius at least 10 per cent larger than r_{80} and an area comparable to the cluster aperture; of these, all but one showed an improvement in their growth curves, and are labelled with a quality flag of 2. For the remaining cluster – RX J0530.5–5852, labelled with a quality flag of 3 – the count rate was estimated by extrapolation of the point on its growth curve with the highest signal-to-noise ratio value; the measured value accounts for 48 per cent of this extrapolated flux. The count rates listed in Table 1 refer to the values after correcting for the flux outside the measurement aperture and in any regions excluded due to the presence of point sources (the conversion factor is typically 30 per cent). All fluxes and luminosities are calculated using this extrapolated value.

The conversion from count rate to flux and luminosity used the same spectral model as for the simulations (a 6-keV thermal bremsstrahlung model, Section 2.6), with the Galactic column densities for each cluster taken from the compilation of Marshall &

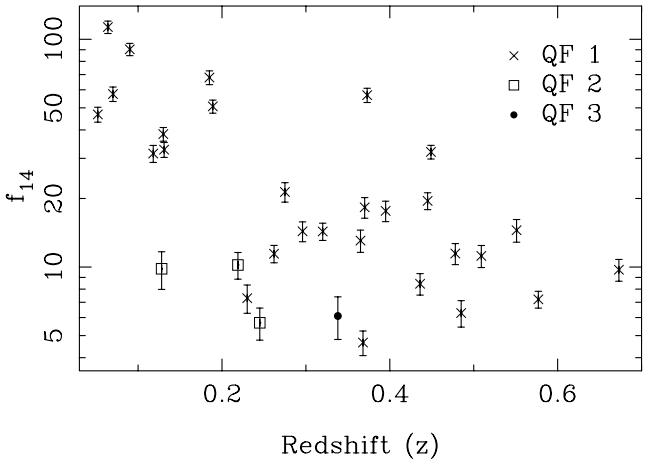

Figure 11. Flux–redshift distribution of the Southern SHARC catalogue. Fluxes (f_{14}) are given in units of 10^{-14} erg cm^{-2} s^{-1} for the observed 0.5–2.0 keV passband, and the symbol types indicate the quality flag (the QF column in Table 1) assigned to the radial profile for the cluster.

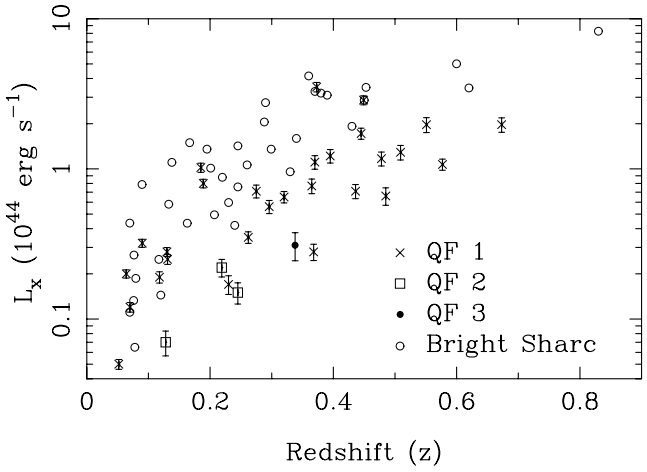

Figure 12. Cluster X-ray luminosities, in the rest-frame 0.5–2.0 keV passband, of the Southern SHARC catalogue, where the symbol types are as in Fig. 11. Also shown, as the open circles, are the clusters from the Bright SHARC catalogue (Romer et al. 2000).

Clark (1984). The luminosities were calculated for both the 0.5–2.0 and 0.3–3.5 keV passbands, and are listed in Table 1 along with a fractional error calculated by adding, in quadrature, the Poisson error on the number of detected counts and a 5 per cent error to account for the use of a single cluster temperature (Section 2.6). The error is generally dominated by the first term, due to the small number of counts detected in most sources. Figs 11 and 12 show the distribution of fluxes and luminosities with redshift of the Southern SHARC catalogue. As expected from the simulations (Section 2.7), at high redshift the catalogue is restricted to moderate- and low-luminosity clusters.

The method used to measure cluster fluxes is designed for high-redshift clusters, where the projected core radius, and hence the correction factor, does not change significantly with redshift. A consequence of this is that the fluxes, and hence luminosities, reported for the low-redshift sources – in particular the group-like systems – are likely to be overestimated. For instance, for a group with a core radius of 50 kpc, the use of a 250-kpc core radius causes the flux to

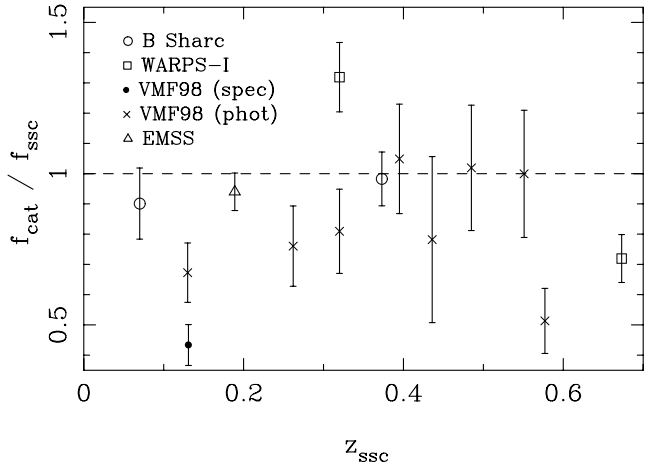

Figure 13. Comparison of flux estimates of the cluster catalogues, where z_{ssc} and f_{ssc} are the redshift and flux values from the Southern SHARC catalogue and f_{cat} the flux from one of the Bright SHARC, WARPS-I, VMF98 or EMSS catalogues. For the EMSS and WARPS-I points the error bars indicate the error from only the Southern Sharc measurement, whereas for the other catalogues they represent the combined error (the errors represent the 68.3 per cent confidence limit).

be overestimated by 20 per cent. At higher redshifts, Fig. 10 shows that the correction to total fluxes is not strongly dependent upon the parameters of the profile, although the use of a constant core radius can lead to systematic uncertainties of a similar size to the flux error (e.g. Romer et al. 2000).

Fig. 13 shows how the flux measurements of the common clusters from the various cluster samples compare with those of the Southern SHARC catalogue. The error bars indicate the 1σ confidence limits on the flux ratio: they are lower limits for the EMSS and WARPS-I points since only the error on the Southern SHARC flux measurement was used. RX J2108.8–0517, at $z = 0.32$, is the only cluster detected in more than one comparison catalogue. The differences in flux are large, with the Southern SHARC measurement (1.43×10^{-13} erg cm^{-2} s^{-1}) being roughly mid-way between that of VMF98 (1.16×10^{-13} erg cm^{-2} s^{-1}) and WARPS-I (1.89×10^{-13} erg cm^{-2} s^{-1}). Part of the discrepancy for this cluster may be due to differences in the algorithms used to exclude flux from nearby sources (A. Vikhlinin, private communication).

For the high-redshift ($z \geqslant 0.3$) sample, the average value of the ratio f_{cat}/f_{ssc} is 0.9 ± 0.2. A change of 10 per cent does not significantly affect the derived XLF and is typical of the variations seen between the cluster surveys (Nichol et al. 1997; Jones et al. 1998; Romer et al. 2000; Perlman et al. 2002).

4 DISCUSSION

The number–flux distribution of the Southern SHARC survey is shown in Fig. 14 as solid circles and the dashed line indicates the no-evolution prediction based on the low-redshift cluster XLF of Ebeling et al. (1997). Also displayed as open squares and the solid line are the results of Gioia et al. (2001) and Jones et al. (1998), respectively. The differences between these three surveys are typical of those found when comparing all the high-redshift *ROSAT* cluster catalogues, as shown by fig. 2 of Gioia et al. (2001).

Burke et al. (1997) used the $1/V_a$ method (Avni & Bahcall 1980) to estimate the Southern SHARC XLF for the $z = 0.3$–0.7 redshift shell. The XLF has been recomputed using the method advocated by

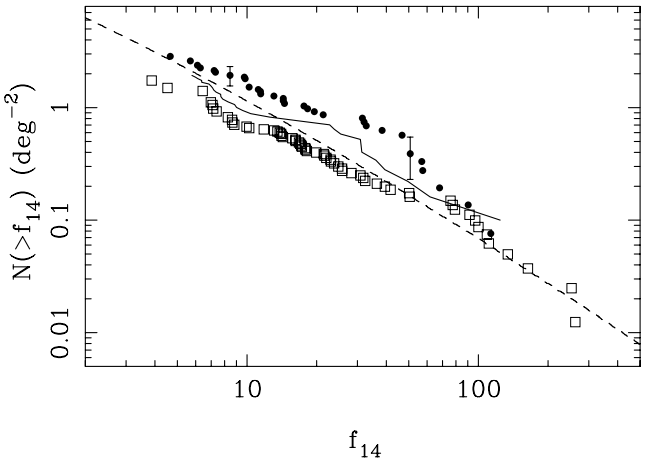

Figure 14. Solid points show the number–flux distribution for the 32 clusters presented in Table 1. The flux (f_{14}) is in the 0.5–2.0 keV energy band and has units of 10^{-14} erg cm^{-2} s^{-1}. The solid line indicates the WARPS-I values from Jones et al. (1998), the open squares those from the NEP survey (Gioia et al. 2001) and the dashed line the no-evolution prediction using the XLF of Ebeling et al. (1997). Error bars, calculated assuming Poisson statistics, are displayed for two points at fluxes close to 5×10^{-13} and 9×10^{-14} erg cm^{-2} s^{-1}.

Table 2. Southern SHARC XLF for $z = 0.3$–0.7.

log L_R	N_c	log $n(L_R)$ $1/V_a$	log $n(L_R)$ PC	Error	
43.5	2	−5.52	−5.70	+0.37	−0.45
43.8	4	−6.26	−6.25	+0.25	−0.28
44.1	6	−6.61	−6.63	+0.20	−0.22
44.4	4	−7.17	−7.17	+0.25	−0.28

Luminosities, L_R, are in units of 10^{44} erg s^{-1} in the 0.5–2.0 keV range and the luminosity bins were chosen to have a width of $\Delta\log L_R = 0.3$ and positioned so that there were at least two clusters per bin (N_c). The XLF values (n) are taken from Burke et al. (1997) for the $1/V_a$ column and calculated using the method of Page & Carrera (2000) for the PC column; the units of n are 10^{-7} Mpc^{-3} (10^{44} erg s^{-1})$^{-1}$. Poisson errors (1σ) are from Gehrels (1986).

Page & Carrera (2000), since the $1/V_a$ method can bias the result for luminosity bins in which the survey selection function varies strongly. Table 2 lists the results of the two calculations; although the values change slightly, there is no significant difference in the result.

The implications of this sample in the context of cluster evolution have been presented in Collins et al. (1997) and Burke et al. (1997); in agreement with other surveys (e.g. Nichol et al. 1997; Jones et al. 1998; Vikhlinin et al. 1998b; Nichol et al. 1999; Rosati et al. 2000), the number density of low-luminosity ($L_x \sim 10^{44}$ erg s^{-1}) clusters is consistent with little, or no, evolution out to $z \sim 0.5$. The consistency of results between the surveys suggests that there are no significant differences in the various detection algorithms employed, so any biases – such as those highlighted by Pesce et al. (1990) – are likely to be at a low level.

Recently, Henry (2002) has shown that it is necessary to combine several cluster samples to measure any evolution in the XLF at luminosities around 10^{44} erg s^{-1}. Such an amalgamation requires an understanding of any systematic differences between the samples. As highlighted by Section 3.2 (see also, Nichol et al. 1997; Jones et al. 1998; Romer et al. 2000; Perlman et al. 2002), the fluxes of the different surveys agree overall to ∼10 per cent, although variations in individual measurements can be significantly larger. While some of the discrepancy in the cluster fluxes is due to the methods used to extrapolate the measured value to account for flux outside the source aperture (e.g. Fig. 10 and Romer et al. 2000), more sensitive X-ray observations of the clusters are required. Observations of high-redshift clusters from the Southern and Bright SHARC catalogues by *XMM–Newton*, as part of the XMM–Newton Ω project (Lumb et al. 2003), provide accurate measurements of the cluster surface-brightness profiles and luminosities (e.g. Arnaud et al. 2002), and so can be used to address the reasons for the differences in the flux estimates, as well as to indicate whether the extrapolation schemes used by the *ROSAT* surveys to estimate the total cluster fluxes from the measured values are too simplistic (Jones et al. 1998; Henry 2000; Romer et al. 2000).

When combining samples it is also important to understand why a particular survey fails to detect clusters (e.g. Adami et al. 2000). The Southern SHARC catalogue was matched with the Bright SHARC, VMF98 and WARPS-I lists, looking for clusters detected in only one catalogue. A radius of 1 arcmin around each cluster was used and the search was restricted to the common areas of each PSPC field: the Southern SHARC uses the whole field out to a radius of 18 arcmin except for those regions listed in Table A1; the Bright SHARC excluded regions within 150 arcsec of the field centre; VMF98 was taken to use the area between 2 and 17.5 arcmin; and WARPS-I used the 3–15 arcmin region. The comparison was limited to clusters with redshifts greater than 0.2 since the Southern SHARC catalogue was not designed to accurately categorize low-redshift systems (Section 3.2). There are no Bright SHARC catalogue clusters that are missing from the Southern SHARC sample, and those found only in Table 1 are too faint to be included in the Bright SHARC survey. The VMF98 catalogue contains one cluster candidate ([VMF98] 215, $z_{ph} = 0.21$) which is not found in the Southern SHARC, while it misses three high-redshift Southern SHARC clusters (RX J0505.3–2849, RX J0530.5–5852 and RX J1205.0–0333): RX J0505.3–2849 was missed because it was split into two sources (A. Vikhlinin, private communication) while the remaining two clusters are too faint to be included in the VMF98 source list. Finally, the WARPS-I catalogue contains one source from the main catalogue (WARP J2320.7+1659, a blend of a $z = 1.8$ AGN and a $z = 0.5$ cluster) and one cluster from the non-statistical sample (WARP J2108.6–0507 at $z = 0.222$ with possible point-source contamination) that are not included in the Southern SHARC sample, while it does not miss any from Table 1. Thus clusters missing from the Southern SHARC catalogue either have no spectroscopic confirmation or show evidence for flux contamination.

5 CONCLUSIONS

This paper presents the Southern SHARC catalogue, a deep, small-area survey for X-ray-emitting high-redshift clusters of galaxies in serendipitous *ROSAT* PSPC observations. The fields were chosen so that moderate luminosity clusters (∼10^{44} erg s^{-1}) could be detected out to $z \sim 0.5$: the 66 fields that met these criteria cover an area of 17.7 deg^2 after masking out the targets of the observation.

Since galaxy clusters are a small fraction of the X-ray detections in *ROSAT* observations, selection was restricted to those sources that were significantly extended. The list of extended sources contains 96 entries; optical follow-up – involving imaging and multi-object

spectroscopy – together with a literature search identifies all but eight of these sources. The catalogue is 92 per cent identified and contains 32 clusters, the majority of which have at least three spectroscopic redshifts. The high-redshift sample contains 16 clusters in the redshift range $z = 0.3$–0.7 and with X-ray luminosities of between 2×10^{43} and 4×10^{44} erg s^{-1}. The results are, in general, in good agreement with those of other surveys for those fields that are in common. The properties of the high-redshift sample are consistent with there being no evolution in the cluster XLF at luminosities $\sim 10^{44}$ erg s^{-1}.

ACKNOWLEDGMENTS

DJB would like to thank the following for their valuable input during the survey: Pat Henry, Brad Holden, David Allen, Harald Ebeling, Laurence Jones and Richard Bower. DJB acknowledges the support of SAO contract to SV4-64008 and NASA contract no NAS8-39073 (CXC), and the support and software provided by the Starlink Project which is run by CCLRC on behalf of PPARC. This work is based on observations made with ESO Telescopes at the La Silla Observatory under programme IDs 55.A-0480 and 56.A-0180, with the Anglo-Australian Telescope, and the William Herschel Telescope, which is operated on the island of La Palma by the Isaac Newton Group in the Spanish Observatorio del Roque de los Muchachos of the Instituto de Astrofisica de Canarias. This research has made use of data obtained from the Leicester Database and Archive Service at the Department of Physics and Astronomy, Leicester University, UK, and the NASA/IPAC Extragalactic Database (NED), which is operated by the Jet Propulsion Laboratory, California Institute of Technology, under contract with the National Aeronautics and Space Administration. The Digitized Sky Surveys were produced at the Space Telescope Science Institute under US Government grant NAG W-2166. The images of these surveys are based on photographic data obtained using the Oschin Schmidt Telescope on Palomar Mountain and the UK Schmidt Telescope.

REFERENCES

Abell G.O., Corwin H.G., Olowin R.P., 1989, ApJS, 70, 1
Adami C., Ulmer M.P., Romer A.K., Nichol R.C., Holden B.P., Pildis R.A., 2000, ApJS, 131, 391
Allan D.J., Vallance R.J., 1995, Starlink User Note, 98.6, Rutherford Appleton Laboratory
Almaini O., Shanks T., Boyle B.J., Griffiths R.E., Roche N., Stewart G.C., Georgantopoulos I., 1996, MNRAS, 282, 295
Aragón-Salamanca A., Ellis R.S., Couch W.J., Carter D., 1993, MNRAS, 262
Arnaud M. et al., 2002, A&A, 390, 27
Avni Y., Bahcall J.N., 1980, ApJ, 235, 694
Bahcall N.A., Soneira R.M., 1983, ApJ, 270, 20
Bennett C.L. et al., 1996, ApJ, 464, L1
Boese F.G., 2000, A&AS, 141, 507
Böhringer H. et al., 2000, ApJS, 129, 435
Bower R.G., 1997, MNRAS, 288, 355
Bower R.G., Lucey J.R., Ellis R.S., 1992, MNRAS, 254, 589
Briel U.G. et al., 1994, ROSAT Users' Handbook. MPE, Garching
Brown R.L., Gould R.J., 1970, Phys. Rev. D, 1, 2252
Burke D.J., 1997, PhD thesis, Univ. Durham
Burke D.J., Collins C.A., Sharples R.M., Romer A.K., Holden B.P., Nichol R.C., 1997, ApJ, 488, L83
Cash W., 1979, ApJ, 228, 939
Castander F.J. et al., 1995, Nat, 377, 39
Collins C.A., Burke D.J., Romer A.K., Sharples R.M., Nichol R.C., 1997, ApJ, 479, L117
Collins C.A. et al., 2000, MNRAS, 319, 939
Cruddace R.G., Hasinger G., Trümper J., Schmidt J.H.M.M., Hartner G.D., Rosso C., Snowden S.L., 1991, Exp. Astron., 1, 365
David L.P., Slyz A., Jones C., Forman W., Vrtilek S.D., Arnaud K.A., 1993, ApJ, 412, 479
de Grandi S. et al., 1999a, ApJ, 514, 148
de Grandi S. et al., 1999b, ApJ, 513, L17
Ebeling H., Voges W., Böhringer H., Edge A.C., Huchra J.P., Briel U.G., 1996, MNRAS, 281, 799
Ebeling H., Edge A.C., Fabian A.C., Allen S.W., Crawford C.S., Böhringer H., 1997, ApJ, 479, L101
Ebeling H., Edge A.C., Bohringer H., Allen S.W., Crawford C.S., Fabian A.C., Voges W., Huchra J.P., 1998, MNRAS, 301, 881
Ebeling H., Edge A.C., Allen S.W., Crawford C.S., Fabian A.C., Huchra J.P., 2000, MNRAS, 318, 333
Ebeling H., Edge A.C., Henry J.P., 2000, AAS/High Energy Astrophysics Division, 32, 1803
Edge A.C., Stewart G.C., Fabian A.C., Arnaud K.A., 1990, MNRAS, 245, 559
Eke V.R., Cole S., Frenk C.S., 1996, MNRAS, 282, 263
Ellis S.C., Jones L.R., 2002, MNRAS, 330, 631
Ettori S., Fabian A.C., 1999, MNRAS, 305, 834
Evrard A.E., 1997, MNRAS, 292, 289
Fairley B.W., Jones L.R., Scharf C., Ebeling H., Perlman E., Horner D., Wegner G., Malkan M., 2000, MNRAS, 315, 669
Frenk C.S., White S.D.M., Efstathiou G., Davis M., 1990, ApJ, 351, 10
Gehrels N., 1986, ApJ, 303, 336
Georgantopoulos I., Stewart G.C., Shanks T., Boyle B.J., Griffiths R.E., 1996, MNRAS, 280, 276
Gioia I.M., Luppino G.A., 1994, ApJS, 94, 583
Gioia I.M., Maccacaro T., Schild R.E., Wolter A., Stocke J.T., Morris S.L., Henry J.P., 1990, ApJS, 72, 567
Gioia I.M., Henry J.P., Mullis C.R., Voges W., Briel U.G., Böhringer H., Huchra J.P., 2001, ApJ, 553, L105
Grego L., Carlstrom J.E., Reese E.D., Holder G.P., Holzapfel W.L., Joy M.K., Mohr J.J., Patel S., 2001, ApJ, 552, 2
Hasinger G., Burg R., Giacconi R., Schmidt M., Trumper J., Zamorani G., 1998, A&A, 329, 482
Heavens A.F., 1993, MNRAS, 263
Henry J.P., 2000, ApJ, 534, 565
Henry J.P., 2002, in Bowyer S., Hwang C.-Y., eds, ASP Conf. Ser., Matter and Energy in Clusters of Galaxies. Astron. Soc. Pac., San Francisco, to appear (astro-ph/0207148)
Henry J.P., Arnaud K.A., 1991, ApJ, 372, 410
Henry J.P., Gioia I.M., Maccacaro T., Morris S.L., Stocke J.T., Wolter A., 1992, ApJ, 386, 408
Hogg D.W., Pahre M.A., McCarthy J.K., Cohen J.G., Blandford R., Smail I., Soifer B.T., 1997, MNRAS, 288, 404
Jones C., Forman W., 1999, ApJ, 511, 65
Jones L.R., Scharf C., Ebeling H., Perlman E., Wegner G., Malkan M., Horner D., 1998, ApJ, 495, 100
Kaiser N., 1984, ApJ, 284, L9
Kaiser N., 1986, MNRAS, 222, 323
Lazzati D., Campana S., Rosati P., Panzera M.R., Tagliaferri G., 1999, ApJ, 524, 414
Lewis A.D., Stocke J.T., Ellingson E., Gaidos E.J., 2002, ApJ, 566, 744
Lumb D.H. et al., 2003, A&A, submitted
Marshall F.J., Clark G.W., 1984, ApJ, 287
Mason K.O. et al., 2000, MNRAS, 311, 456
McHardy I.M. et al., 1998, MNRAS, 295, 641
Mittaz J.P.D. et al., 1999, MNRAS, 308, 233
Mohr J.J., Mathiesen B., Evrard A.E., 1999, ApJ, 517, 627
Moretti A. et al., 2001, in Cristiani S., Renzini A., Williams R.E., eds, Proc. ESO/ECF/STScI Workshop, Deep Fields. Springer-Verlag, Heidelberg, p. 207
Morrison R., McCammon D., 1983, ApJ, 270, 119
Nichol R.C., Briel O.G., Henry J.P., 1994, MNRAS, 267, 771

Nichol R.C. et al., 1999, ApJ, 521, L21
Nichol R.C., Holden B.P., Romer A.K., Ulmer M.P., Burke D.J., Collins C.A., 1997, ApJ, 481, 644
Page M.J., Carrera F.J., 2000, MNRAS, 311, 433
Peacock J.A., West M.J., 1992, MNRAS, 259, 494
Perlman E.S., Horner D.J., Jones L.R., Scharf C.A., Ebeling H., Wegner G., Malkan M., 2002, ApJS, 140, 265
Pesce J.E., Fabian A.C., Edge A.C., Johnstone R.M., 1990, MNRAS, 244, 58
Piccinotti G., Mushotzky R.F., Boldt E.A., Holt S.S., Marshall F.E., Serlemitsos P.J., Shafer R.A., 1982, ApJ, 253, 485
Ponman T.J., Allan D.J., Jones L.R., Merrifield M., McHardy I.M., Lehto H.J., Luppino G.A., 1994, Nat, 369, 462
Reblinsky K., Bartelmann M., 1999, A&A, 345, 1
Reichart D.E., Nichol R.C., Castander F.J., Burke D.J., Romer A.K., Holden B.P., Collins C.A., Ulmer M.P., 1999, ApJ, 518, 521
Romer A.K., Collins C.A., Böhringer H., Ebeling H., Cruddace R.C., MacGillivray H.T., 1994, Nat, 372, 75
Romer A.K. et al., 2000, ApJS, 126, 209
Rosati P., della Ceca R., Burg R., Norman C., Giacconi R., 1995, ApJ, 445, L11
Rosati P., Borgani S., della Ceca R., Stanford A., Eisenhardt P., Lidman C., 2000, in Plionis M., Georgantopoulos I., eds, Large Scale Structure in the X-ray Universe. Atlantisciences, Paris, p. 13
Sarazin C.L., 1988, X-ray Emission from Clusters of Galaxies. Cambridge Univ. Press, Cambridge
Scharf C.A., Jones L.R., Ebeling H., Perlman E., Malkan M., Wegner G., 1997, ApJ, 477, 79
Smail I., Hogg D.W., Yan L., Cohen J.G., 1995, ApJ, 449
Smoot G.F. et al., 1992, ApJ, 396, L1
Snowden S.L., McCammon D., Burrows D.N., Mendenhall J.A., 1994, ApJ, 424, 714
Stanford S.A., Eisenhardt P.R., Dickinson M., 1998, ApJ, 492
van Haarlem M.P., Frenk C.S., White S.D.M., 1997, MNRAS, 287, 817
Vikhlinin A., Forman W., Jones C., Murray S., 1995, ApJ, 451, 564
Vikhlinin A., McNamara B.R., Forman W., Jones C., Quintana H., Hornstrup A., 1998a, ApJ, 502, 558
Vikhlinin A., McNamara B.R., Forman W., Jones C., Quintana H., Hornstrup A., 1998b, ApJ, 498, L21
Vikhlinin A., Forman W., Jones C., 1999, ApJ, 525, 47
Vikhlinin A., McNamara B.R., Hornstrup A., Quintana H., Forman W., Jones C., Way M., 1999, ApJ, 520, L1
White N.E., Giommi P., Angelini L., 1994, IAU Circular, 6100, 1

APPENDIX A: *ROSAT* OBSERVATIONS

Table A1. *ROSAT* observations used in the Southern SHARC survey.

Field name	ROR	*S*	$T_{\rm exp}$	$n_{\rm H}$	Field centre		*x*, *y*, *r*	*x*, *y*, *r*
HCG 22	800566	B	12 210	2.92	$03^{\rm h}\,03^{\rm m}\,31\overset{\rm s}{.}2$	$-15^\circ\,40'\,48''$	+2.00, −2.22, 6.0	
MARANO FIELD	701036	BV	44 925	1.79	$03^{\rm h}\,15^{\rm m}\,09\overset{\rm s}{.}6$	$-55^\circ\,13'\,48''$		
A 3112	800555	B	12 354	5.67	$03^{\rm h}\,17^{\rm m}\,57\overset{\rm s}{.}6$	$-02^\circ\,57'\,00''$		
J1780 (5BL)	800371	B	20 651	2.25	$03^{\rm h}\,23^{\rm m}\,12\overset{\rm s}{.}0$	$-51^\circ\,05'\,24''$	+0.00, +0.00, 4.8	
J2175 (23C)	800367	B	14 795	2.33	$03^{\rm h}\,32^{\rm m}\,57\overset{\rm s}{.}6$	$-39^\circ\,06'\,36''$	+0.02, −0.20, 4.8	
EXO 033319−2554.	300079	BVW	47 278	1.57	$03^{\rm h}\,37^{\rm m}\,55\overset{\rm s}{.}2$	$-25^\circ\,21'\,00''$		
QSF3	900632	BV	43 552	1.67	$03^{\rm h}\,42^{\rm m}\,12\overset{\rm s}{.}0$	$-44^\circ\,07'\,48''$		
F 1557	800171	B	20 467	5.02	$04^{\rm h}\,12^{\rm m}\,55\overset{\rm s}{.}2$	$-65^\circ\,51'\,00''$	+0.00, +0.00, 4.8	
NGC 1553/49	600623	B	14 547	2.07	$04^{\rm h}\,15^{\rm m}\,28\overset{\rm s}{.}8$	$-55^\circ\,37'\,12''$	+2.33, +1.75, 3.6	+5.79, −9.51, 4.8
NGC 1566	600456	B	16 520	1.86	$04^{\rm h}\,20^{\rm m}\,00\overset{\rm s}{.}0$	$-54^\circ\,56'\,24''$	+0.26, +0.15, 4.8	
RX J0453.4−4214	300221	BV	11 754	2.13	$04^{\rm h}\,53^{\rm m}\,26\overset{\rm s}{.}3$	$-42^\circ\,13'\,48''$	−0.03, +0.19, 3.0	
NGC 1705	600436	B	21 861	2.12	$04^{\rm h}\,54^{\rm m}\,14\overset{\rm s}{.}4$	$-53^\circ\,21'\,36''$	−0.10, −0.08, 3.0	
MS0459+0327	701557	B	11 285	7.21	$05^{\rm h}\,02^{\rm m}\,07\overset{\rm s}{.}2$	$+03^\circ\,31'\,48''$	+0.51, +0.08, 3.0	
0503−286	700233	BV	17 618	1.73	$05^{\rm h}\,05^{\rm m}\,50\overset{\rm s}{.}4$	$-28^\circ\,35'\,24''$	−0.19, +0.04, 4.8	
J2001 (21C)	800368	B	21 661	2.03	$05^{\rm h}\,13^{\rm m}\,33\overset{\rm s}{.}6$	$-48^\circ\,18'\,36''$	+0.00, +0.00, 3.6	
RX J0529.4−5855	300130	BV	13 649	3.26	$05^{\rm h}\,29^{\rm m}\,28\overset{\rm s}{.}7$	$-58^\circ\,54'\,36''$	+0.00, −0.25, 3.0	
HR 2550	200638		10 390	5.92	$06^{\rm h}\,48^{\rm m}\,12\overset{\rm s}{.}0$	$-61^\circ\,55'\,48''$	−0.11, −0.89, 4.8	
F1767 (10TC)	800370	B	16 836	3.72	$08^{\rm h}\,47^{\rm m}\,40\overset{\rm s}{.}7$	$+17^\circ\,54'\,00''$	+0.38, −1.02, 4.8	
3C212	700436	BV	20 060	4.26	$08^{\rm h}\,58^{\rm m}\,40\overset{\rm s}{.}8$	$+14^\circ\,09'\,00''$	+0.09, +0.55, 3.0	
NGC 2992	701458	B	17 700	5.23	$09^{\rm h}\,45^{\rm m}\,43\overset{\rm s}{.}2$	$-14^\circ\,19'\,48''$	−0.23, +0.28, 4.8	
3C227	701587	BV	10 633	4.02	$09^{\rm h}\,47^{\rm m}\,45\overset{\rm s}{.}6$	$+07^\circ\,25'\,12''$	+0.00, +0.17, 3.0	
HCG42	800359	B	12 437	5.20	$10^{\rm h}\,00^{\rm m}\,21\overset{\rm s}{.}6$	$-19^\circ\,39'\,00''$	−1.71, +0.95, 7.2	
09595−0755	600178	BV	13 374	5.80	$10^{\rm h}\,02^{\rm m}\,00\overset{\rm s}{.}0$	$-08^\circ\,09'\,36''$	−0.06, −0.25, 3.0	
PG1034+001	201243	BV	17 394	4.79	$10^{\rm h}\,37^{\rm m}\,04\overset{\rm s}{.}8$	$-00^\circ\,08'\,24''$	−0.20, +0.07, 3.0	
J1834 (5BC/8BL/2	800366	B	17 991	3.80	$10^{\rm h}\,46^{\rm m}\,04\overset{\rm s}{.}8$	$-00^\circ\,24'\,00''$	−13.74, −6.54, 3.0	+14.30, −3.20, 4.8
11395+1033	600420	B	11 412	1.80	$11^{\rm h}\,42^{\rm m}\,09\overset{\rm s}{.}6$	$+10^\circ\,16'\,48''$	+0.25, −0.25, 3.0	
NGC 3923	600113		14 693	6.06	$11^{\rm h}\,51^{\rm m}\,02\overset{\rm s}{.}4$	$-28^\circ\,48'\,36''$	−0.17, +0.40, 4.8	
MS1158.6−0323	701202	BV	13 134	3.38	$12^{\rm h}\,01^{\rm m}\,14\overset{\rm s}{.}3$	$-03^\circ\,40'\,48''$	−0.02, −0.11, 3.0	
PG1159−035	201367	BV	30 589	3.51	$12^{\rm h}\,04^{\rm m}\,25\overset{\rm s}{.}7$	$-03^\circ\,40'\,19''$		
GROUP 1	800421	B	13 732	2.01	$12^{\rm h}\,14^{\rm m}\,21\overset{\rm s}{.}6$	$+13^\circ\,05'\,24''$	+0.00, +0.00, 5.0	
MK 49	600166	B	11 567	1.89	$12^{\rm h}\,19^{\rm m}\,09\overset{\rm s}{.}6$	$+03^\circ\,51'\,36''$	+0.76, +0.23, 3.0	
NGC 4410	600587	B	16 987	1.75	$12^{\rm h}\,26^{\rm m}\,28\overset{\rm s}{.}8$	$+09^\circ\,01'\,12''$	−0.19, +0.00, 3.0	
NGC 4569	600437	B	17 368	1.68	$12^{\rm h}\,36^{\rm m}\,48\overset{\rm s}{.}0$	$+13^\circ\,10'\,12''$	+0.50, −0.38, 4.8	
EX HYDRAE	300093	BV	14 726	6.86	$12^{\rm h}\,52^{\rm m}\,24\overset{\rm s}{.}0$	$-29^\circ\,15'\,00''$	+0.00, +0.00, 4.8	
3C 277.2	800393	B	12 781	2.07	$12^{\rm h}\,53^{\rm m}\,33\overset{\rm s}{.}5$	$+15^\circ\,42'\,36''$	−0.12, −0.12, 4.8	
ABELL 3535	800374	B	10 932	6.69	$12^{\rm h}\,58^{\rm m}\,26\overset{\rm s}{.}3$	$-28^\circ\,26'\,24''$	−8.31, −2.81, 6.0	

Table A1 – *continued*

Field name	ROR	*S*	T_{exp}	n_H	Field centre		*x*, *y*, *r*	*x*, *y*, *r*
A 3537	800384	B	11 255	5.58	$13^h\ 01^m\ 02\overset{s}{.}4$	$-32°\ 26'\ 24''$	−0.25, −0.01, 6.0	
RX J1313.3−3259	300219	B	13 447	5.07	$13^h\ 13^m\ 16\overset{s}{.}7$	$-32°\ 59'\ 24''$	+0.00, +0.07, 3.0	
13224−3809	600419	B	18 845	5.33	$13^h\ 25^m\ 19\overset{s}{.}2$	$-38°\ 24'\ 36''$	−0.06, −0.36, 1.8	
M83	600188		22 221	4.69	$13^h\ 37^m\ 00\overset{s}{.}0$	$-29°\ 52'\ 12''$	+0.17, +0.29, 8.4	
J1836 (3CR/23T)	800369	B	17 228	3.14	$13^h\ 44^m\ 04\overset{s}{.}8$	$-00°\ 10'\ 48''$	−14.79, +10.00, 4.8	+14.02, −9.22, 4.8
HCG67	800637	B	14 980	2.78	$13^h\ 49^m\ 02\overset{s}{.}4$	$-07°\ 12'\ 36''$	+2.54, +0.23, 6.0	
PKS 1351−018	701500	BV	14 335	3.99	$13^h\ 54^m\ 07\overset{s}{.}2$	$-02°\ 05'\ 59''$	−0.07, +0.00, 3.0	
MKN 841	700257	BV	16 399	2.83	$15^h\ 04^m\ 02\overset{s}{.}4$	$+10°\ 26'\ 24''$	−0.30, +0.00, 3.0	
PZ TEL	201597	B	21 465	6.33	$18^h\ 53^m\ 04\overset{s}{.}7$	$-50°\ 10'\ 48''$	+0.07, −0.03, 3.0	
RE1938−46	300272	B	21 234	5.09	$19^h\ 35^m\ 48\overset{s}{.}0$	$-46°\ 40'\ 48''$		
PKS 2005−489	700488	BV	11 415	4.57	$20^h\ 09^m\ 26\overset{s}{.}3$	$-48°\ 49'\ 48''$	−0.25, +0.03, 4.8	
E2034−228	700547	BV	11 250	4.60	$20^h\ 37^m\ 31\overset{s}{.}2$	$-22°\ 42'\ 36''$	−0.98, +0.00, 3.0	
AE AQR	300218	BW	20 344	5.98	$20^h\ 38^m\ 14\overset{s}{.}3$	$-01°\ 21'\ 00''$		
HD 197890	201374	BV	28 778	6.07	$20^h\ 47^m\ 45\overset{s}{.}6$	$-36°\ 35'\ 24''$	−0.17, −0.33, 3.0	
IC5063	700538	B	18 671	4.83	$20^h\ 52^m\ 02\overset{s}{.}4$	$-57°\ 04'\ 12''$	−0.05, +0.04, 3.0	
RE2107–05	300389	BVW	28 105	5.00	$21^h\ 07^m\ 55\overset{s}{.}2$	$-05°\ 16'\ 12''$	+0.65, −1.50, 3.0	
PAVO FIELD	900133	BV	22 522	3.03	$21^h\ 14^m\ 24\overset{s}{.}0$	$-67°\ 47'\ 24''$		
UKRO-287-1	800336	B	13 431	2.22	$21^h\ 39^m\ 07\overset{s}{.}1$	$-42°\ 51'\ 36''$	+0.00, +0.00, 5.0	
A 2397	800344		12 867	4.65	$21^h\ 56^m\ 04\overset{s}{.}8$	$+01°\ 19'\ 48''$	+1.01, +3.76, 7.8	
HICKSON 90	800419	B	12 964	1.59	$22^h\ 02^m\ 04\overset{s}{.}8$	$-31°\ 58'\ 12''$	+0.59, −1.07, 6.0	
MT FIELD	700516	BV	22 370	2.69	$22^h\ 03^m\ 04\overset{s}{.}8$	$-18°\ 55'\ 12''$		
23016–5144	600177	BV	14 480	1.57	$23^h\ 04^m\ 36\overset{s}{.}0$	$-51°\ 28'\ 12''$	+0.36, +0.40, 3.0	
MCG-2-58-22	701250	BVW	16 617	3.54	$23^h\ 04^m\ 43\overset{s}{.}2$	$-08°\ 41'\ 24''$	+0.09, +0.35, 3.0	
GLIESE 887	201339	BV	10 497	2.10	$23^h\ 05^m\ 24\overset{s}{.}0$	$-35°\ 52'\ 12''$	+0.02, −0.09, 3.0	
GRB790406	400144	BV	18 910	1.71	$23^h\ 14^m\ 00\overset{s}{.}0$	$-49°\ 39'\ 36''$	+0.32, +0.30, 3.0	
RX J2316.1−0527	300220	BVW	13 649	3.78	$23^h\ 16^m\ 02\overset{s}{.}4$	$-05°\ 27'\ 00''$	+0.28, +0.00, 3.0	
III ZW 102	600439	BVW	10 569	3.95	$23^h\ 20^m\ 31\overset{s}{.}2$	$+17°\ 13'\ 48''$	−0.06, −0.05, 3.0	
MS2340.9−1511	701205	BVW	11 356	2.37	$23^h\ 43^m\ 31\overset{s}{.}2$	$-14°\ 55'\ 12''$	−0.62, −0.30, 3.0	
HCG97	800357		12 050	3.57	$23^h\ 47^m\ 26\overset{s}{.}3$	$-02°\ 18'\ 36''$	−0.84, +0.59, 7.2	
F1637 (23TL)	800372	B	16 223	1.56	$23^h\ 59^m\ 16\overset{s}{.}7$	$-32°\ 17'\ 24''$	+0.00, +0.00, 4.8	

Fields are identified by their names, which are taken from the header of the events lists, the identification number of the *ROSAT* observation (ROR) and the equatorial coordinates of the central position of the observation, given in equinox 2000. The column *S* indicates whether these fields are also in the B Sharc (B), VMF98 (V) or WARPS-I (W) surveys. The exposure times, Texp, refer to the cleaned exposure time (Section 2.4.1) of the observation, and are in units of seconds. The column labelled n_H lists the Galactic hydrogen column density of the field centre, taken from the compilation of Marshall & Clark (1984), and is in units of 10^{20} cm^{-2}. The remaining columns indicate those regions of the field excluded from the survey, as described in Section 2.3: the *x*, *y* and *r* values give the position and radius of the circular region excluded from the survey (they are in arcmin, with north and east as the positive directions).

APPENDIX B: EXTENDED SOURCES

Table B1. Extended sources in the Southern SHARC survey.

Name	ROR	RA	Dec.	ID	*z*	Notes
RX J0313.4–5510	701036	$03^h\ 13^m\ 29\overset{s}{.}7$	$-55°\ 10'\ 25\overset{''}{.}7$	LA	1.378	1SAX J0313.5–5509, 1WGA J0313.4–5509
RX J0314.9–5458	701036	$03^h\ 14^m\ 55\overset{s}{.}8$	$-54°\ 57'\ 47\overset{''}{.}3$	LQ	–	[GZd97] 1.4GHz 37
RX J0318.2–0301	800555	$03^h\ 18^m\ 17\overset{s}{.}4$	$-03°\ 01'\ 14\overset{''}{.}7$	SC	0.370(1)	BS J0318.2–0301, NVSS J031816–030159
RX J0318.5–0303	800555	$03^h\ 18^m\ 32\overset{s}{.}8$	$-03°\ 02'\ 45\overset{''}{.}7$	SC	0.373(3)	BS J0318.5–0302
RX J0322.5–5101	800371	$03^h\ 22^m\ 33\overset{s}{.}9$	$-51°\ 00'\ 53\overset{''}{.}4$	P	–	1WGA J0322.5–5100
RX J0323.8–5114	800371	$03^h\ 23^m\ 50\overset{s}{.}4$	$-51°\ 14'\ 23\overset{''}{.}3$	M	–	
RX J0323.8–5116	800371	$03^h\ 23^m\ 49\overset{s}{.}0$	$-51°\ 15'\ 45\overset{''}{.}3$	–	–	
RX J0333.0–3914	800367	$03^h\ 33^m\ 05\overset{s}{.}5$	$-39°\ 13'\ 49\overset{''}{.}4$	SC	0.245(5)	
RX J0333.8–3906	800367	$03^h\ 33^m\ 50\overset{s}{.}1$	$-39°\ 06'\ 23\overset{''}{.}5$	(LC)	–	(RX J0334.0–3901)
RX J0334.0–3901	800367	$03^h\ 34^m\ 03\overset{s}{.}2$	$-39°\ 00'\ 48\overset{''}{.}7$	LC	0.064	Abell 3135
RX J0334.1–3904	800367	$03^h\ 34^m\ 11\overset{s}{.}0$	$-39°\ 03'\ 54\overset{''}{.}1$	(LC)	–	(RX J0334.0–3901)
RX J0337.4–2519	300079	$03^h\ 37^m\ 28\overset{s}{.}1$	$-25°\ 18'\ 30\overset{''}{.}6$	IP	–	WARP J0337.4–2518
RX J0337.7–2522	300079	$03^h\ 37^m\ 45\overset{s}{.}2$	$-25°\ 22'\ 26\overset{''}{.}2$	SC	0.577(3)	[VMF98] 033, BSe J0337.6–2522
RX J0338.4–2536	300079	$03^h\ 38^m\ 26\overset{s}{.}6$	$-25°\ 36'\ 23\overset{''}{.}6$	LA	0.334	MS 0336.3–2546, 1WGA J0338.4–2536
RX J0338.6–2532	300079	$03^h\ 38^m\ 40\overset{s}{.}7$	$-25°\ 32'\ 00\overset{''}{.}1$	IM	–	
RX J0341.8–4353	900632	$03^h\ 41^m\ 52\overset{s}{.}0$	$-43°\ 53'\ 21\overset{''}{.}6$	LA	–	AX J0341.8–4353, 1WGA J0341.8–4353
RX J0342.2–4351	900632	$03^h\ 42^m\ 16\overset{s}{.}0$	$-43°\ 50'\ 51\overset{''}{.}2$	–	–	BSe J0342.2–4350, 1WGA J0342.2–4350
RX J0342.4–4418	900632	$03^h\ 42^m\ 27\overset{s}{.}6$	$-44°\ 18'\ 19\overset{''}{.}6$	–	–	

Table B1 – *continued*

Name	ROR	RA	Dec.	ID	z	Notes
RX J0411.7–6547	800171	$04^h\ 11^m\ 42\overset{s}{.}8$	$-65°\ 46'\ 48''.4$	M	–	BSe J0411.7–6547
RX J0413.7–6603	800171	$04^h\ 13^m\ 44\overset{s}{.}0$	$-66°\ 02'\ 30''.4$	P	–	
RX J0416.7–5525	600623	$04^h\ 16^m\ 44\overset{s}{.}8$	$-55°\ 25'\ 08''.6$	SC	0.365(3)	
RX J0452.7–5316	600436	$04^h\ 52^m\ 44\overset{s}{.}2$	$-53°\ 15'\ 31''.7$	IM	–	1WGA J0452.7–5315
RX J0454.5–4219	300221	$04^h\ 54^m\ 35\overset{s}{.}2$	$-42°\ 19'\ 17''.2$	SA	0.231	
RX J0454.9–4211	300221	$04^h\ 54^m\ 54\overset{s}{.}2$	$-42°\ 11'\ 03''.9$	SS	star	1WGA J0454.9–4211
RX J0455.7–5314	600436	$04^h\ 55^m\ 45\overset{s}{.}0$	$-53°\ 13'\ 31''.5$	IP	–	1WGA J0455.7–5312
RX J0505.3–2849	700233	$05^h\ 05^m\ 19\overset{s}{.}9$	$-28°\ 49'\ 05''.2$	SC	0.509(3)	
RX J0505.6–2828	700233	$05^h\ 05^m\ 36\overset{s}{.}7$	$-28°\ 27'\ 56''.1$	IM	–	
RX J0505.9–2826	700233	$05^h\ 05^m\ 57\overset{s}{.}6$	$-28°\ 25'\ 56''.0$	LC	0.131	[VMF98] 038, 1WGA J0505.9–2825
RX J0505.9–2841	700233	$05^h\ 05^m\ 59\overset{s}{.}4$	$-28°\ 40'\ 38''.0$	MP	–	[VMF98] 039, BSe J0506.0–2841
RX J0514.3–4827	800368	$05^h\ 14^m\ 18\overset{s}{.}4$	$-48°\ 27'\ 02''.5$	SA	0.230	BS J0514.2–4826
RX J0529.6–5848	300130	$05^h\ 29^m\ 39\overset{s}{.}9$	$-58°\ 48'\ 20''.7$	IM	–	[VMF98] 043
RX J0529.6–5852	300130	$05^h\ 29^m\ 39\overset{s}{.}4$	$-58°\ 51'\ 37''.1$	M	–	
RX J0530.5–5852	300130	$05^h\ 30^m\ 31\overset{s}{.}1$	$-58°\ 51'\ 34''.8$	SC	0.338(2)	
RX J0857.8+1410	700436	$08^h\ 57^m\ 48\overset{s}{.}4$	$+14°\ 09'\ 57''.1$	LQ	0.178	RIXOS F250_014, BSe J0857.8+1410
RX J0857.8+1411	700436	$08^h\ 57^m\ 52\overset{s}{.}2$	$+14°\ 10'\ 41''.5$	MP	–	
RX J0858.4+1357	700436	$08^h\ 58^m\ 25\overset{s}{.}3$	$+13°\ 57'\ 14''.6$	SC	0.485(3)	[VMF98] 066, RIXOS F250_057, 1WGA J0858.4+1357
RX J0945.6–1434	701458	$09^h\ 45^m\ 40\overset{s}{.}5$	$-14°\ 34'\ 06''.2$	IP	–	BS J0945.6–1434
RX J0946.5–1410	701458	$09^h\ 46^m\ 32\overset{s}{.}9$	$-14°\ 09'\ 50''.5$	SC	0.230(5)	
RX J0947.8+0741	701587	$09^h\ 47^m\ 48\overset{s}{.}8$	$+07°\ 41'\ 24''.7$	SQ	0.631	[VMF98] 075, BS J0947.8+0741
RX J0947.9+0730	701587	$09^h\ 47^m\ 57\overset{s}{.}5$	$+07°\ 30'\ 26''.0$	SC	0.128(3)	NVSS J094755+073021
RX J0948.3+0729	701587	$09^h\ 48^m\ 20\overset{s}{.}9$	$+07°\ 28'\ 58''.7$	IP	–	
RX J1001.1–1926	800359	$10^h\ 01^m\ 09\overset{s}{.}3$	$-19°\ 26'\ 23''.7$	LG	–	ESO 567−1 G003
RX J1002.6–0809	600178	$10^h\ 02^m\ 40\overset{s}{.}2$	$-08°\ 08'\ 48''.1$	P	–	[VMF98] 083, 1WGA J1002.6–0808, NVSS J100236–080834
RX J1036.4+0002	201243	$10^h\ 36^m\ 26\overset{s}{.}5$	$+00°\ 02'\ 06''.2$	IP	–	
RX J1037.9–0007	201243	$10^h\ 37^m\ 57\overset{s}{.}6$	$-00°\ 06'\ 53''.3$	SQ	0.746	
RX J1045.3–0017	800366	$10^h\ 45^m\ 23\overset{s}{.}2$	$-00°\ 16'\ 50''.3$	SS	star	
RX J1141.7+1022	600420	$11^h\ 41^m\ 45\overset{s}{.}5$	$+10°\ 21'\ 47''.8$	SQ	1.250	BSe J1141.7+1021
RX J1142.0+1009	600420	$11^h\ 42^m\ 05\overset{s}{.}6$	$+10°\ 08'\ 47''.5$	LC	0.118	Abell 1354, 1WGA J1142.0+1009
RX J1142.2+1027	600420	$11^h\ 42^m\ 16\overset{s}{.}8$	$+10°\ 26'\ 47''.1$	LC	0.070	Abell 1356, BS J1142.2+1026
RX J1200.8–0328	701202	$12^h\ 00^m\ 48\overset{s}{.}4$	$-03°\ 27'\ 50''.9$	SC	0.395(4)	[VMF98] 111, RIXOS F222_504, BSe J1200.8–0327
RX J1203.4–0350	201367	$12^h\ 03^m\ 26\overset{s}{.}4$	$-03°\ 49'\ 58''.1$	IP	–	1WGA J1203.4–0350
RX J1204.3–0351	201367	$12^h\ 04^m\ 22\overset{s}{.}8$	$-03°\ 50'\ 59''.8$	SC	0.262(5)	[VMF98] 113, BSe J1204.3–0351, 1WGA J1204.3–0351
RX J1205.0–0333	201367	$12^h\ 05^m\ 02\overset{s}{.}8$	$-03°\ 32'\ 31''.1$	SC	0.368(5)	BSe J1205.0–0332
RX J1213.8+1311	800421	$12^h\ 13^m\ 52\overset{s}{.}6$	$+13°\ 10'\ 36''.2$	LG	0.008	NGC 4193, BSe J1213.8+1310, 1WGA J1213.8+1310
RX J1227.1+0856	600587	$12^h\ 27^m\ 07\overset{s}{.}9$	$+08°\ 55'\ 57''.3$	(SC)	–	(RX J1227.2+0858)
RX J1227.2+0858	600587	$12^h\ 27^m\ 14\overset{s}{.}5$	$+08°\ 58'\ 10''.1$	SC	0.090(4)	
RX J1236.4+1259	600437	$12^h\ 36^m\ 25\overset{s}{.}5$	$+12°\ 58'\ 59''.1$	G	–	1WGA J1236.4+1259
RX J1252.0–2921	300093	$12^h\ 52^m\ 04\overset{s}{.}6$	$-29°\ 20'\ 42''.6$	–	–	[VMF98] 124
RX J1253.2+1556	800393	$12^h\ 53^m\ 14\overset{s}{.}7$	$+15°\ 55'\ 52''.7$	SC	0.275(4)	BSe J1253.2+1556
RX J1313.6–3251	300219	$13^h\ 13^m\ 39\overset{s}{.}1$	$-32°\ 50'\ 44''.3$	SC	0.052(2)	BS J1313.6–3250
RX J1325.0–3814	600419	$13^h\ 25^m\ 01\overset{s}{.}6$	$-38°\ 13'\ 35''.3$	SC	0.296(6)	BSe J1325.0–3814, 1WGA J1325.0–3813
RX J1325.5–3826	600419	$13^h\ 25^m\ 34\overset{s}{.}8$	$-38°\ 25'\ 49''.5$	SC	0.445(4)	BSe J1325.6–3825, 1WGA J1325.5–3825
RX J1338.0–2944	600188	$13^h\ 38^m\ 05\overset{s}{.}8$	$-29°\ 44'\ 25''.3$	LC	0.189	MS 1335.2−2928
RX J1354.2–0222	701500	$13^h\ 54^m\ 17\overset{s}{.}2$	$-02°\ 21'\ 45''.9$	SC	0.551(5)	[VMF98] 151, NVSS J135417–022213
RX J1936.1–4640	300272	$19^h\ 36^m\ 06\overset{s}{.}9$	$-46°\ 40'\ 04''.1$	P	–	
RX J2038.4–0125	300218	$20^h\ 38^m\ 29\overset{s}{.}3$	$-01°\ 25'\ 16''.8$	SC	0.673(2)	WARP J2038.4–0125
RX J2048.7–3640	201374	$20^h\ 48^m\ 45\overset{s}{.}4$	$-36°\ 39'\ 52''.8$	M	–	
RX J2050.6–5700	700538	$20^h\ 50^m\ 41\overset{s}{.}6$	$-56°\ 59'\ 39''.6$	IP	–	
RX J2052.2–5654	700538	$20^h\ 52^m\ 12\overset{s}{.}2$	$-56°\ 54'\ 26''.6$	P	–	1AXG J205208–5653
RX J2053.8–5710	700538	$20^h\ 53^m\ 51\overset{s}{.}2$	$-57°\ 09'\ 41''.1$	G	–	
RX J2053.9–5709	700538	$20^h\ 53^m\ 55\overset{s}{.}0$	$-57°\ 09'\ 09''.2$	M	–	
RX J2106.8–0510	300389	$21^h\ 06^m\ 49\overset{s}{.}0$	$-05°\ 09'\ 54''.8$	SC	0.449(7)	1WGA J2106.8–0509, 1AXG J210648–0510
RX J2107.7–0526	300389	$21^h\ 07^m\ 47\overset{s}{.}7$	$-05°\ 26'\ 11''.6$	MP	–	
RX J2108.2–0514	300389	$21^h\ 08^m\ 15\overset{s}{.}6$	$-05°\ 13'\ 44''.1$	P	–	1WGA J2108.2–0513
RX J2108.8–0517	300389	$21^h\ 08^m\ 49\overset{s}{.}5$	$-05°\ 16'\ 39''.6$	SC	0.320(2)	[VMF98] 200, WARP J2108.8–0516
RX J2114.3–6801	900133	$21^h\ 14^m\ 20\overset{s}{.}8$	$-68°\ 01'\ 04''.2$	LC	0.130	[VMF98] 201, DS 210958–681304, 1WGA J2114.3–6800
RX J2137.6–4249	800336	$21^h\ 37^m\ 40\overset{s}{.}0$	$-42°\ 49'\ 00''.4$	P	–	
RX J2137.8–4251	800336	$21^h\ 37^m\ 49\overset{s}{.}5$	$-42°\ 50'\ 49''.1$	SC	0.185(7)	Abell 3791
RX J2137.8–4253	800336	$21^h\ 37^m\ 53\overset{s}{.}2$	$-42°\ 52'\ 49''.2$	(SC)	–	(RX J2137.8–4251)
RX J2138.3–4253	800336	$21^h\ 38^m\ 18\overset{s}{.}9$	$-42°\ 53'\ 20''.5$	MP	–	1WGA J2138.3–4254
RX J2138.7–4245	800336	$21^h\ 38^m\ 42\overset{s}{.}8$	$-42°\ 44'\ 35''.6$	–	–	

Table B1 *– continued*

Name	ROR	RA	Dec.	ID	z	Notes
RX J2138.8–4301	800336	$21^h\,38^m\,52\overset{s}{.}2$	$-43^\circ\,01'\,05\overset{''}{.}6$	P	–	
RX J2139.5–4302	800336	$21^h\,39^m\,31\overset{s}{.}5$	$-43^\circ\,01'\,50\overset{''}{.}5$	P	–	
RX J2155.9+0109	800344	$21^h\,55^m\,59\overset{s}{.}1$	$+01^\circ\,09'\,02\overset{''}{.}1$	SC	0.219(6)	
RX J2155.9+0110	800344	$21^h\,55^m\,54\overset{s}{.}9$	$+01^\circ\,10'\,03\overset{''}{.}9$	(SC)	–	(RX J2155.9+0109)
RX J2201.3–3155	800419	$22^h\,01^m\,19\overset{s}{.}0$	$-31^\circ\,54'\,33\overset{''}{.}8$	M	–	
RX J2202.4–3204	800419	$22^h\,02^m\,29\overset{s}{.}4$	$-32^\circ\,04'\,10\overset{''}{.}9$	SS	star	1WGA J2202.4–3204
RX J2202.5–3208	800419	$22^h\,02^m\,32\overset{s}{.}8$	$-32^\circ\,07'\,56\overset{''}{.}9$	P	–	RBS 1816, 1AXG J220232–3207
RX J2202.7–1902	700516	$22^h\,02^m\,44\overset{s}{.}6$	$-19^\circ\,01'\,59\overset{''}{.}8$	SC	0.436(3)	[VMF98] 205
RX J2305.0–5114	600177	$23^h\,05^m\,03\overset{s}{.}2$	$-51^\circ\,13'\,38\overset{''}{.}7$	P	–	
RX J2305.4–3546	201339	$23^h\,05^m\,25\overset{s}{.}1$	$-35^\circ\,45'\,40\overset{''}{.}3$	–	–	[VMF98] 214, BSe J2305.4–3545
RX J2313.0–4951	400144	$23^h\,13^m\,04\overset{s}{.}0$	$-49^\circ\,51'\,18\overset{''}{.}8$	–	–	BSe J2313.1–4950, 1WGA J2313.0–4953
RX J2313.2–4933	400144	$23^h\,13^m\,17\overset{s}{.}1$	$-49^\circ\,33'\,20\overset{''}{.}3$	P	–	
RX J2314.2–4955	400144	$23^h\,14^m\,15\overset{s}{.}8$	$-49^\circ\,55'\,17\overset{''}{.}8$	–	–	1WGA J2314.2–4955
RX J2315.4–0542	300220	$23^h\,15^m\,28\overset{s}{.}2$	$-05^\circ\,41'\,43\overset{''}{.}7$	MP	–	
RX J2359.5–3211	800372	$23^h\,59^m\,35\overset{s}{.}9$	$-32^\circ\,11'\,06\overset{''}{.}5$	SC	0.478(3)	BSe J2359.5–3211

The 96 extended sources detected by the Southern SHARC survey. The ROR column identifies the field in which the source was detected (Table A1). The coordinates refer to the centre of the X-ray source and are equinox 2000 with a typical error of 10 arcsec. The ID column lists the identification of the source. The first letter – if it is one of L, S, or I – refers to how the source was identified: L for from the literature (the NASA Extragalactic Database); an S indicates the source was spectroscopically identified; an I means that the identification was based on the *R*-band image taken at the ESO 3.6-m telescope; otherwise the Digital Sky Survey image was used. The second letter lists which class of object the source belongs to: a C means a cluster; a G a galaxy; a Q for a QSO; an A for an AGN; and an S for a star. The letter P shows those sources for which an optical point source lies close to, or at, the centre of the X-ray emission; this source is taken to be the X-ray-emitting object. The letter M refers to those cases where the extended X-ray emission is actually from multiple point sources. An ID of – means that the source remains unidentified, and parentheses around the ID show that the source lies within 1 Mpc of the cluster identified in the Notes column. The column z lists the redshifts of the sources, obtained either from the literature, or during the optical follow-up described in Section 3.1. For those clusters identified during this follow-up, i.e. those with an ID of SC, the listed redshift is the average value of all the galaxies measured for that cluster, where the number in parentheses gives the number of such galaxies. The Notes column indicates other identifications for these sources (using a search radius of 1 arcmin): the main catalogues referred to are Romer et al. (2000) for BS and BSe (for sources that are in Appendix E only), Vikhlinin et al. (1998a) for [VMF98], Mason et al. (2000) for RIXOS, Perlman et al. (2002) for WARP, White, Giommi & Angelini (1994) for 1WGA, and the Abell catalogue (Abell, Corwin & Olowin 1989). Several clusters are found close to clusters with similar redshifts: RX J0318.2–0301 and RX J0318.5–0303 ($z = 0.37$) are 4.1 arcmin apart; RX J1227.2+0858 is 8.0 arcmin from Abell 1541 ($z = 0.089$); and RX J2359.5–3211 is 7.5 arcmin from F1637.23TL (a cluster at $z = 0.48$).

This paper has been typeset from a TEX/LATEX file prepared by the author.